Title

Timing of mid-crustal ductile extension in the northern Snake Range metamorphic core complex, Nevada: Evidence from U/Pb zircon ages

Journal

Geosphere, 13(2)

ISSN

1553-040X

Authors

Lee, Jeffrey
Blackburn, Terrence
Johnston, Scott

Publication Date

2017-04-01

DOI

10.1130/ges01429.1

Peer reviewed

Research Paper

GEOSPHERE

GEOSPHERE; v. 13, no. 2

doi:10.1130/GES01429.1

10 figures; 3 tables

CORRESPONDENCE: jeff@geology.cwu.edu

CITATION: Lee, J., Blackburn, T., and Johnston, S., Timing of mid-crustal ductile extension in the northern Snake Range metamorphic core complex, Nevada: Evidence from U/Pb zircon ages: Geosphere, v. 13, no. 2, p. 439–459, doi:10.1130/GES01429.1.

Received 16 September 2016
Revision received 6 January 2017
Accepted 13 February 2017
Published online 17 March 2017

Timing of mid-crustal ductile extension in the northern Snake Range metamorphic core complex, Nevada: Evidence from U/Pb zircon ages

Jeffrey Lee[1], Terrence Blackburn[2], and Scott Johnston[3]

[1]Department of Geological Sciences, Central Washington University, 400 E. University Way, Ellensburg, Washington 98926, USA
[2]Department of Earth and Planetary Sciences Department, University of California, 1156 High Street, Santa Cruz, California 95064, USA
[3]Physics Department, California Polytechnic State University, Building 180, Room 204, San Luis Obispo, California 93407, USA

ABSTRACT

Metamorphic core complexes within the western U.S. record a history of Cenozoic ductile and brittle extensional deformation, metamorphism, magmatism, and exhumation within the footwalls of high-angle Basin and Range normal faults. In models proposed for the formation of metamorphic core complexes there is a close temporal and spatial link between upper crustal normal faulting, lower crustal ductile extension and flow, and detachment faulting. To provide constraints on the timing of ductile extension in the northern Snake Range metamorphic core complex (Nevada) and thereby test these models, we present new ^{238}U-^{206}Pb dates on zircons from both deformed and undeformed rhyolite dikes intruded into this core complex. The older age bracket is from the northern dike swarm, which was emplaced in the northwestern part of the range pretectonic to syntectonic with ductile extension. The younger age bracket is from the Silver Creek dike swarm, which was emplaced in the southern part of the range after ductile extensional deformation. The ^{238}U-^{206}Pb zircon ages from these dikes provide tight bounds on the timing of ductile extension, between 37.806 ± 0.051 Ma and 22.49 ± 0.36 Ma. Our field observations, petrography, and ^{238}U-^{206}Pb zircon ages on these dikes combined with published data on the geology and kinematics of extension, moderate- and low-temperature thermochronology on lower plate rocks, and age and faulting histories of Cenozoic sedimentary basins, are interpreted as recording an episode of localized upper crustal brittle extension during the late Eocene that drove upward ductile extensional flow of hot middle crustal rocks from beneath the northern Snake Range detachment soon after, or simultaneously with, emplacement of the older dike swarm. Exhumation of the lower plate continued in a rolling hinge–isostatic rebound style; the western part of the lower plate was exhumed first and the eastern part extended ductilely either episodically or continuously until the latest Oligocene–earliest Miocene, when the post-tectonic younger dike swarm was emplaced. Major brittle slip along the eastern part of the northern Snake Range detachment and along high-angle normal faults exhumed the lower plate during middle Miocene.

INTRODUCTION

Metamorphic core complexes within the U.S. Cordillera (Fig. 1) record a complex history of ductile and brittle extensional deformation associated with metamorphism and magmatism, and final exhumation within the footwalls of high-angle Basin and Range normal faults. These core complexes are characterized by a domal geometry and a low-angle, normal slip detachment fault that juxtaposes a hanging wall of generally unmetamorphosed upper crustal sedimentary and volcanic rocks cut by high-angle normal faults from a footwall of ductilely extended middle crustal metasedimentary and metaigneous rocks. There are two groups of ages of these core complexes in the U.S. Cordillera; an older Paleogene group north of the Snake River Plain and a younger late Paleogene to Neogene group south of the Snake River Plain (Konstantinou and Miller, 2015, and references therein) (Fig. 1).

Although the structural, metamorphic, intrusive, and exhumation histories and tectonic significance of metamorphic core complexes have been topics of research for more than 40 years, there remains disagreement about: (1) whether the detachment faults that bound these complexes formed and moved at low angles or initiated at high angles and rotated to a low angle during slip; (2) whether brittle and ductile extensional deformation were linked in space and time; (3) the temporal relationship of both modes of extension to the development of the detachment fault; and (4) the fundamental tectonic and physical processes that drove the formation of the metamorphic core complexes (e.g., Wernicke, 1981; Miller et al., 1983; Coney and Harms, 1984; Lister and Davis, 1989; Jackson, 1987; Wernicke and Axen, 1988; Buck, 1988; Lee, 1995; Henry et al., 2011; Konstantinou et al., 2012; Wells et al., 2012; Vogel et al., 2012; Konstantinou and Miller, 2015).

The northern Snake Range metamorphic core complex, east-central Nevada (Figs. 2 and 3), has been central to the debate on the origin and evolution of metamorphic core complexes; there has been disagreement regarding the age of the high-strain fabrics in the footwall of the detachment fault, their spatial-temporal relation to the overlying detachment fault and

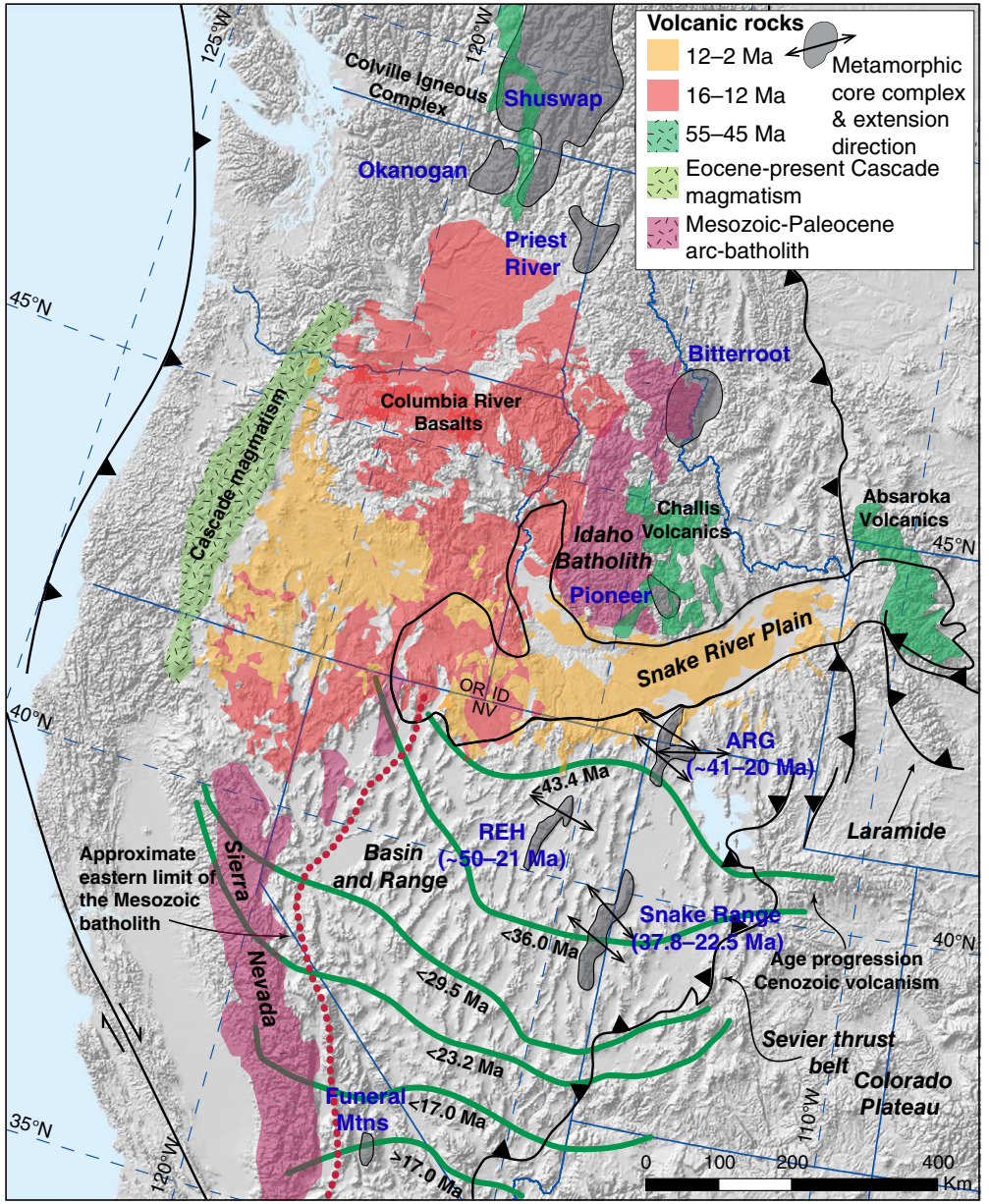

Figure 1. Map of western North America showing the location of major tectonic features, magmatic provinces, and metamorphic core complexes. ARG—Albion–Raft River–Grouse Creek Mountains; REH—Ruby–East Humboldt Mountains. Modified from Konstantinou et al. (2012).

to hanging-wall extension, and the origin and slip history along the detachment fault (cf. Wernicke, 1981; Miller et al., 1983; Bartley and Wernicke, 1984; Lee et al., 1987; Lister and Davis, 1989; Lee and Sutter, 1991; Lee, 1995; Miller et al., 1999a; Cooper et al., 2010a; Gébelin et al., 2011, 2014). Based on muscovite and potassium feldspar $^{40}Ar/^{39}Ar$ studies, combined with structural and quartz petrofabric investigations, it was suggested (Lee et al., 1987; Lee and Sutter, 1991; Lee, 1995) that the ductile extension deformation was diachronous, Eocene in age on the west flank and ending in the early Miocene on the east flank, and related to normal slip along the detachment fault, the northern Snake Range décollement (NSRD). More recent muscovite $^{40}Ar/^{39}Ar$ studies in lower plate rocks, combined with stable isotope studies, reached similar conclusions regarding the timing of ductile extension and relation to slip along the NSRD, with the added interpretation that surface fluids reached the upper part of the lower plate on the east flank during the ductile extension in the early Miocene (Gébelin et al., 2011, 2014). Based on a combination of kinematic, paleomagnetic, and geothermometry data from the northeastern flank of this core complex, Cooper et al. (2010a) argued that extensional mylonites from the dome core, which formed between late Eocene and early Miocene, predated slip along the detachment fault, and were subsequently captured and exhumed in the footwall of the NSRD. Low-temperature thermochronology results from apatite and zircon fission track data across the lower plate led Miller et al. (1999a) to suggest that, in contrast to the interpretations above, ductile extension in the lower plate may have occurred during the middle Miocene as the lower plate was exhumed from depths at which ductile extension occurred toward the Earth's surface in the footwall of the brittle NSRD, and during a time when flanking Paleogene and Neogene basins formed.

In almost all of the models proposed for formation of detachment faults and metamorphic core complexes (see following), i.e., those based on the geometry and kinematics of extensional deformation (e.g., Miller et al., 1983; Buck, 1988), two-dimensional (2D) thermal mechanical models (e.g., Rey et al., 2009a, 2009b), three-dimensional (3D) analogue models (e.g., Brun et al., 1994; Tirel et al., 2006), and energy constrained models (Rosenbaum et al., 2005), there is a close temporal and spatial link between upper crustal normal faulting, lower crustal ductile extension and flow, and detachment faulting. Thus, tight constraints on the timing of ductile extensional deformation compared to the timing of upper crustal normal faulting and slip along the detachment fault are key to addressing these issues and for testing models proposed for formation of metamorphic core complexes. In this paper we report new ^{238}U-^{206}Pb zircon ages on dikes that are pre–ductile extension, syn–ductile extension, and post–ductile extension in the lower plate of the northern Snake Range metamorphic core complex that place more precise bounds on the timing of mylonitic ductile extensional deformation in the lower plate. These data bracket ductile extension to between late Eocene to latest Oligocene–earliest Miocene and, combined with published work on the timing of upper crustal normal and detachment faulting, have implications for the mechanism by which this metamorphic core complex formed.

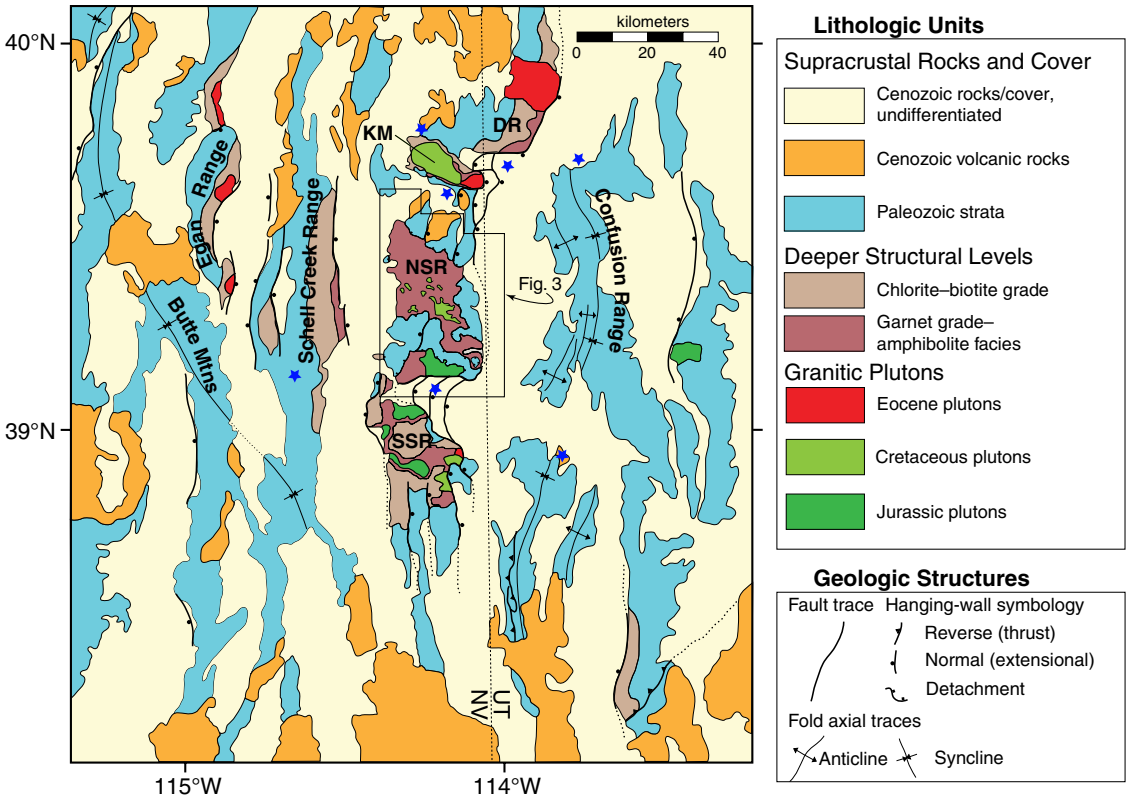

Figure 2. Simplified geologic map of east-central Nevada (NV) showing location of the northern Snake Range (NSR) and Paleogene and Neogene sedimentary basins discussed in the text (blue stars) (modified after Miller and Gans, 1989). DR—Deep Creek Range; KM—Kern Mountains; SSR—southern Snake Range; UT—Utah.

METAMORPHIC CORE COMPLEX MODELS

Early mechanisms and concepts proposed for the formation of metamorphic core complexes suggested that they represented a ductile-brittle transition zone, a low-angle normal fault, and the result of a combination of a rolling hinge and isostatic rebound (e.g., Miller et al., 1983; Wernicke, 1981; Lister and Davis, 1989; Buck, 1988; Wernicke and Axen, 1988) (Fig. 4). These models were based on field observations and centered on the geometry and kinematics of extensional deformation, particularly the geometry and slip history along the detachment fault. The models were based on the assumption that the detachment fault initiated at the onset of extension and that slip along the fault occurred at the same time as brittle faulting in the upper plate and ductile extension in the lower plate. In the low-angle normal fault and isostatic rebound models (Figs. 4B, 4C), ductile extension beneath or in an extensional shear zone at the toe of the detachment fault mostly drove exhumation of the ductilely extended footwall. In the rolling hinge model (Fig. 4C), the detachment fault initiated at a high angle, but during slip, the fault flexed and rotated to a shallower dip in response to extensional denudation of the hanging wall and isostatic unloading of the footwall (Buck, 1988; Wernicke and Axen, 1988). In this model, extension in the upper crust was accommodated by upward flow of lower crust into the region of thinned crust, implying high temperatures in the lower crust, potentially high enough to generate partial melts, that reduced viscosity sufficiently to accommodate flow. This basic concept, i.e., reduced viscosity that accommodates flow, is essential to rheologic models for core complexes.

The 2D thermal-mechanical numerical models provided insight into the interplay among plate boundary forces, internal forces, heat (i.e., rheology), extensional strain rates, and exhumation in the development of metamorphic core complexes and detachment faults (e.g., Lavier et al., 1999, 2000; Wijns et al., 2005; Rosenbaum et al., 2005; Tirel et al., 2008; Rey et al., 2009a, 2009b, 2011; Whitney et al., 2013). For example, Whitney et al. (2013) presented a model whereby horizontal extension of thick continental crust (60 km) and no partial melting (i.e., a cool geothermal gradient) resulted in widespread normal faulting in the upper crust and homogeneously distributed ductile extension in

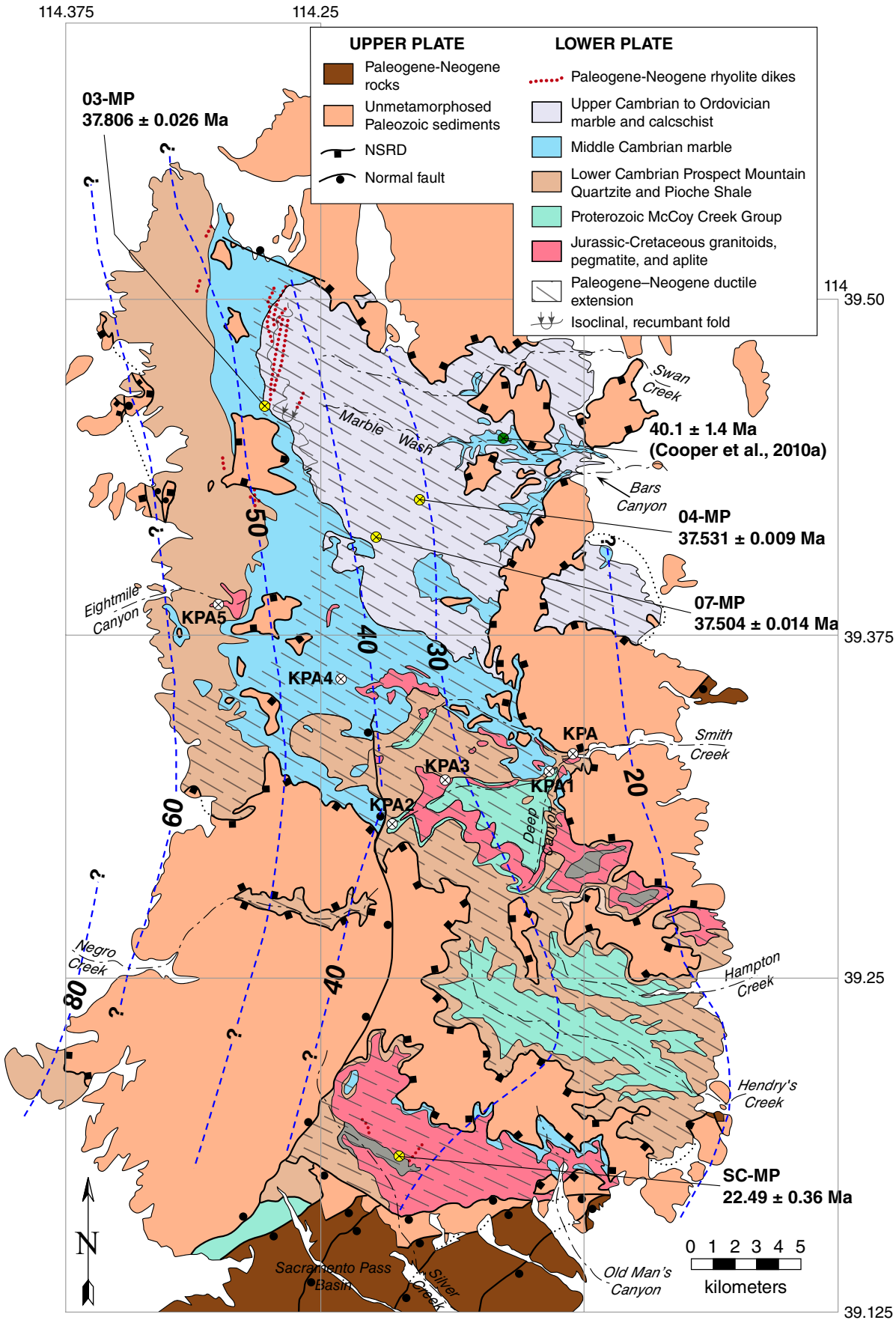

Figure 3. Simplified geologic map of the northern Snake Range metamorphic core complex showing locations of U/Pb zircon samples (yellow circles, this study; green circle, Cooper et al., 2010a) and potassium feldspar (collected from a pegmatite and aplite dike swarm) $^{40}Ar/^{39}Ar$ diffusion domain samples (white circles, Lee, 1995), and contours of muscovite K-Ar and $^{40}Ar/^{39}Ar$ total gas ages (blue dashed lines; modified from Lee and Sutter, 1991). NSRD—northern Snake Range décollement. Map simplified from Gans et al. (1999a, 1999b), Lee et al. (1999a, 1999b), Lee and Gans (1999), Miller et al. (1999b), and Miller and Gans (1999). See Figure 2 for location of the map.

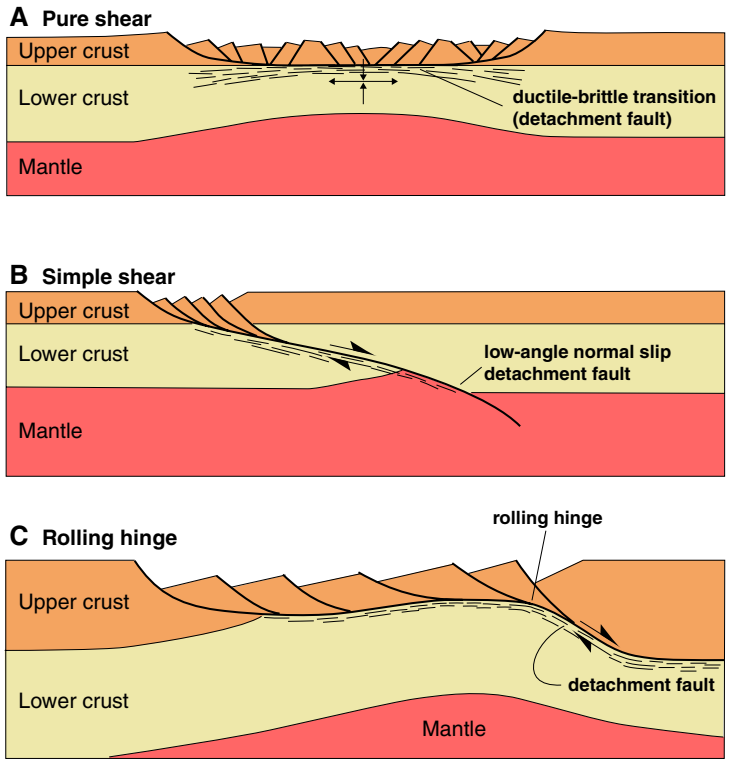

Figure 4. Schematic cross sections showing the geometry of popular early mechanisms and concepts proposed for the formation of metamorphic core complexes. (A) The pure shear ductile-brittle transition model (Miller et al., 1983). (B) The low-angle normal fault simple shear model (Wernicke, 1981). (C) The rolling hinge–isostatic rebound model (e.g., Buck, 1988; Wernicke and Axen, 1988).

the lower crust, whereas a high geothermal gradient resulted in localized normal faulting in the upper crust spatially linked to ductile extension in the lower plate. Models that include variable, boundary driven extensional strain rates (analogous to plate driven extension), the presence of melt, and a local heterogeneity in the upper crust (a preexisting normal fault) yield different crystallization versus exhumation histories (Rey et al., 2009a, 2009b). Fast extension resulted in cooling and crystallization of a migmatite after most of the extension-driven exhumation of the dome in the footwall of a detachment fault, and in weakly deformed, low-pressure migmatites in the dome cores. Slow extension resulted in cooling and crystallization of the migmatite before most of the extension-driven exhumation of the dome in the footwall of the detachment fault, and in strongly deformed, high-pressure migmatites in the dome core. Melt-present experiments resulted in bulk pure shear deformation of the dome except in the vicinity of the detachment fault, whereas melt-absent experiments resulted in bulk simple shear deformation.

The 3D analogue models also shed light on the formation of metamorphic core complexes (e.g., Brun et al., 1994; Tirel et al., 2006; Corti et al., 2003). For example, low strain rates and a low viscosity-density anomaly (simulating a zone of partial melt or a granitic intrusion) in the lower crust or upper mantle facilitates formation of metamorphic core complexes, whereas in the absence of an anomaly, the upper crust and lower crust extend nearly homogeneously.

To generate a metamorphic core complex in both 2D numerical and 3D analogue models, strain localization along an anomaly, such as (1) a preexisting fault (e.g., Buck, 1988; Lavier et al., 1999; Gessner et al., 2007), (2) a large density contrast across the brittle-ductile transition (e.g., Wijns et al., 2005), or (3) a rheologically weak zone (e.g., Brun et al., 1994; Tirel et al., 2006) is required. In contrast, the Rosenbaum et al. (2005) 2D numerical extensional model, based on energy feedback and localization within continental crust, shows that in the absence of a local anomaly, core complex–like faults can develop as a consequence of energy fluxes associated with feedback between rheology, shear heating, thermal stress, and stored energy.

GEOLOGY OF THE NORTHERN SNAKE RANGE

The northern Snake Range is a classic metamorphic core complex exposing a gently arched low-angle normal-slip detachment fault, the NSRD, that separates excellent exposures of a brittlely extended, unmetamorphosed upper plate from a ductilely extended (vertically thinned and horizontally stretched) metamorphosed lower plate (Miller et al., 1983; Lee et al., 1987, 1999a, 1999b; Gans et al., 1999a, 1999b; Lee and Gans, 1999; Miller et al., 1999b; Miller and Gans, 1999).

The upper plate is composed of a predominantly carbonate sequence of miogeoclinal middle Cambrian through Permian sedimentary rocks unconformably overlain by Paleogene and Neogene volcanic and clastic sedimentary rocks (Fig. 3). The lower plate is composed of Neoproterozoic through early Cambrian siliciclastic metasediments and middle to late Cambrian marbles and calc-schists, which are intruded by Mesozoic granitoids, pegmatite, and aplite, and Paleogene and Neogene mafic and rhyolite dikes (Fig. 3). Upper plate rocks are deformed by at least two generations of Paleogene–Neogene, dominantly down-to-the-southeast normal faults that sole into or are cut off by the NSRD, and show little evidence for penetrative deformational events (Miller et al., 1983; Johnston, 2000). The strikes of normal faults and dips of hanging-wall and footwall units indicate a west-northwest–east-southeast extension direction. The timing of slip along these normal faults remains poorly constrained, but is at least late Oligocene to Miocene. To the north of the range, normal faults cut and offset a ca. 24.0 Ma rhyolite tuff (Gans et al., 1989) and on the northeast flank of the range Paleogene and Neogene conglomerates, with lower plate clasts that yield middle Miocene apatite fission track ages, dip into an east-dipping normal fault (Miller et al., 1999a).

In contrast, lower plate rocks record a longer tectonic history that encompasses three metamorphic and deformation events. The oldest metamorphic event, M1, is preserved along the southern flank of the range, where Neoproterozoic and early Cambrian siliciclastic metasediments record contact metamorphism associated with the emplacement of a middle Jurassic plutonic complex (Miller et al., 1988). Jurassic deformational fabrics (D1) are preserved elsewhere in east-central Nevada, including in the Schell Creek Range and southern Snake Range (Fig. 2); however, in the northern Snake Range they have been obliterated by strong superposed Cretaceous and Paleogene and Neogene metamorphic and deformational events (Miller et al., 1988).

The second metamorphic event, M2, appears to have affected the entire lower plate, but is best preserved along the eastern side of the range, where a series of mineral-in isograds indicate an increase in metamorphic grade with depth and from south to north (Miller et al., 1988). Quantitative pressure-temperature investigations on Neoproterozoic metapelitic units yield metamorphic pressures of 6–8 kbar and temperatures of 500–650 °C (Lewis et al., 1999; Cooper et al., 2010b) and an increase in metamorphic pressures northward from ~6 kbar (~23 km depth) in Hendry's Creek in the south to ~8 kbar (~30 km depth) in Deep Canyon to the north (Lewis et al., 1999; Cooper et al., 2010b). Metamorphic mineral assemblages indicate that metamorphic grade decreases from east to west across the range. U-Pb and Sm-Nd geochronology data from monazite and zircon, and garnet and feldspar, respectively, indicate that this metamorphic event is between 78 ± 9 Ma and 88 ± 1.4 Ma (Lee and Fischer, 1985; Cooper et al., 2010b). Due to the strong Paleogene and Neogene deformational and metamorphic overprint, D2 deformational fabrics on the east flank of the range associated with this metamorphic event are only locally preserved as inclusion trails in metamorphic porphyroblasts (Miller et al., 1988; Lewis et al., 1999). In the northwestern part of the range, where lower plate Paleogene and Neogene ductile deformation strain decreases and dies out, older west-dipping foliations, north-northwest–south-southeast–trending intersection lineations, minor thrust faults, and a D2 map-scale fold are inferred to be Cretaceous in age (Lee, 1990; Lee et al., 1999a; Lee and Gans, 1999).

The third and final event is characterized by greenschist facies metamorphism (M3) and a strong penetrative deformational (D3) fabric, characterized by development of a subhorizontal mylonitic foliation and west-northwest–east-southeast mineral stretching lineation (parallel to the extension direction in the upper plate). This third event records ductile extension that affects nearly the entire lower plate and has been interpreted as related to exhumation along the NSRD during the Paleogene and Neogene (Miller et al., 1983; Gaudemer and Tapponnier, 1987; Lee et al., 1987; Lee, 1995) (Fig. 3). The M3 metamorphism is characterized by retrograde chlorite, biotite, and muscovite observed in the strain shadows on M2 metamorphic porphyroblasts, and locally partially replacing these porphyroblasts. The D3 deformational fabric is characterized by substantial ductile extensional plane strain that increases across the range from the northwest, where D3 strain dies out and D2 deformational fabrics are present, to the southeast, where lower plate sedimentary units have been thinned to ~10% of their original stratigraphic thickness (X:Z strain of ~100:1) at the mouth of Hendry's Creek (Miller et al., 1983; Lee et al., 1987; Lee, 1990). Finite strain measurements across the lower plate indicated an average of ~250% horizontal ductile extension (Lee et al., 1987) and palinspastic restoration of two generations of normal faults in the upper plate indicated ~450%–500% brittle extension (Miller et al., 1983). Using 250%–500% as an approximate estimate for the average percent of ductile extension parallel to west-northwest–east-southeast across the lower plate in the southern part of the range, from Negro Creek to Hendry's Creek, yields ~15.6–18.2 km of horizontal extension from a preextensional width of ~6.3–3.7 km to a postextensional, present-day width of ~29.1 km. The kinematics of ductile extensional deformation are characterized by dominantly pure shear deformation on the far western flank of the range and top-to-the east strongly noncoaxial strain on the eastern flank (Lee et al., 1987; Gébelin et al., 2011, 2014).

Pre–ductile to syn–ductile extension dikes broadly constrain the time of onset of ductile extension. A mafic dike boudinaged within the D3 extensional foliation in Marble Wash on the northeastern flank of the range yielded a zircon ^{238}U-^{206}Pb emplacement age of 40.4 ± 1.4 Ma (Cooper et al., 2010a) (Fig. 3), providing a maximum age limit for the mylonitic extensional deformation. In the northwestern part of the lower plate a subvertical rhyolite dike swarm (Fig. 3), emplaced after the formation of the D2 isoclinal fold and prior to the D3 mylonitic extensional deformation (Lee and Sutter, 1991; Lee et al., 1999a), yielded a muscovite $^{40}Ar/^{39}Ar$ age of 37.2 ± 0.4 Ma (Lee and Sutter, 1991; age recalculated using a revised age for standard MMhb from Renne et al., 1998). If this $^{40}Ar/^{39}Ar$ age is an intrusive age, as interpreted by Lee and Sutter (1991), then compared to the mafic dike age it provides a younger maximum age limit on the mylonitic extensional deformation in the lower plate.

Comparison of the lower plate cooling histories from muscovite and potassium feldspar $^{40}Ar/^{39}Ar$ and apatite and zircon fission track thermochronologic studies to estimated temperatures of ductile extension based on microstructural, quartz petrofabric, and stable isotopic investigations provide inferences on the timing of ductile extensional deformation. Moderate temperature thermochronologic data from K/Ar and $^{40}Ar/^{39}Ar$ on muscovite, and $^{40}Ar/^{39}Ar$ multiple diffusion domain (MDD) modeling of potassium feldspar exhibit a decrease in ages from the west flank of the range (maximum age of ca. 80 Ma) to the east flank (minimum age of ca. 20 Ma) (Lee et al., 1987; Lee and Sutter, 1991; Lee, 1995; Miller et al., 1999a; Gébelin et al., 2011, 2014) (Fig. 3). Although the muscovite ages older than ca. 40 Ma may record a partial annealing zone, a partial outgassing event, more than one deformation event, or a heterogeneous thermal overprint (see following detailed discussion), the ca. 40–20 Ma age gradient was interpreted as a consequence of diachronous, west to east, exhumation of lower plate rocks from beneath the NSRD, as brittle extension in the upper plate created space into which the lower plate ductilely flowed; this, in turn, was followed by cessation of ductile extension as temperatures dropped below ~300–450 °C (Lee and Sutter, 1991; Lee, 1995). Interpretation of these thermochronologic data suggests that lower plate rocks on the west flank of the range were exhumed to shal-

low crustal levels and ductile extension ceased during the Eocene, whereas lower plate rocks on the east flank were exhumed to shallow crustal levels and ductile extension ceased during the early Miocene (Lee et al., 1987; Lee and Sutter, 1991; Lee, 1995; Gébelin et al., 2011, 2014). Apatite and zircon fission track data from across the lower plate of the northern Snake Range yielded the same age, ca. 17 Ma, within error. Miller et al. (1999a) interpreted this as uniform and rapid exhumation of the lower plate below ~310 °C and 110 °C, respectively, and inferred that the extensional mylonitic fabric, at least in part, may have formed during the middle Miocene. A spatial-temporal reconstruction of the MDD cooling histories and apatite fission track data over the early Oligocene to middle Miocene time frame reveals a rolling hinge–isostatic rebound mechanism for formation of the NSRD and exhumation of lower plate rocks (Lee, 1995).

To place tighter bounds on the high-strain D3 ductile extensional event in the lower plate of the NSRD, we completed zircon U/Pb geochronology on pretectonic to syntectonic and posttectonic rhyolite dikes exposed in the lower plate. The resulting crystallization ages provide firm bounds on the timing of ductile extension in the lower plate of the northern Snake Range and have implications for evolution of the northern Snake Range metamorphic core complex.

U/Pb ZIRCON AGE RESULTS

To determine the age of onset and duration of the D3 mylonitic extensional deformation event exposed in the lower plate of the northern Snake Range metamorphic core complex, we completed U/Pb analyses of zircons collected from four rhyolite dikes exposed in the lower plate, three from the north-northeast–trending Northern dike swarm, which includes one undeformed dike (sample 03-MP) emplaced before ductile extensional deformation and two deformed dikes emplaced before or during ductile extension (samples 04-MP and 07-MP) that have the well-developed D3 mylonitic foliation, and one sample from the northeast-trending Silver Creek dike swarm, which is an undeformed dike emplaced after ductile extension (sample SC-MP) (Fig. 3). The U/Pb geochronology on zircons from sample 03-MP was completed on the SHRIMP-RG (sensitive high-resolution ion microprobe–reverse geometry) at the Stanford–U.S. Geological Survey Microanalytical Center at Stanford University following the analytical routine of Williams (1998). Data were reduced utilizing the SQUID and Isoplot Excel add-ins of Ludwig (2003); weighted average age (±95% confidence, with error in the standard) and mean square of weighted deviates (MSWD) were calculated using ^{207}Pb corrected ^{206}Pb/^{238}U ages of individual analyses. Because zircons from samples 04-MP and 07-MP contained concentrations of U well in excess of 10,000 ppm, the SHRIMP-RG analyses yielded uninterpretable results. Thus, samples 03-MP, 04-MP, and 07-MP were dated by using chemical abrasion (Mattinson, 2005), isotope dilution, and thermal ionization mass spectrometry (CA-ID-TIMS). Zircon U/Pb determinations were made using the EARTHTIME (http://www.earth-time.org/about.html) mixed ^{205}Pb, ^{233}U, ^{235}U (ET535) tracer and measurements were conducted using the IsotopX Phoenix X62 thermal ionization mass spectrometer at the Massachusetts Institute of Technology. Errors reported for these ages include analytical uncertainty; analytical + tracer uncertainties; and analytical + tracer + decay constant uncertainties. Sample SC-MP was analyzed by laser ablation–multicollector–inductively coupled plasma–mass spectrometry (ICP-MS) at the University of Arizona LaserChron Center on the GVI Isoprobe following the procedure of Gehrels et al. (2008). The reported error for sample SC-MP includes 2σ analytical error + 2σ systematic uncertainty. Sample localities, field photographs, and photomicrographs of the dikes, representative zircon cathodoluminescence (CL) images, and age interpretative plots are shown in Figures 3, 5, 6, 7, and 8, respectively; results of U/Pb isotopic analyses are provided in Tables 1–3.

Sample 03-MP

Sample 03-MP is from a medium- to fine-grained rhyolite dike, and was collected from the southern part of a subvertical north-northeast–trending dike swarm, the Northern dike swarm, exposed in the northwestern part of the lower plate (Figs. 3 and 5A). The dike swarm crosscuts the axial surface of a D2 recumbent syncline, developed within the lower plate middle Cambrian to Ordovician marble and calc-schist, and its associated well-developed S2 axial planar foliation, indicating that dike emplacement was after folding (Lee and Sutter, 1991; Lee et al., 1999a). The dike swarm does not have the younger, much weaker S3 ductile extensional foliation and associated west-northwest–east-southeast stretching L3 lineation that crosscuts the fold, and the trend of the swarm is not orthogonal to the L3 stretching lineation. In thin section, the dike consists of a medium- to fine-grained interlocking texture of quartz + feldspar + muscovite, with local radiating sprays of muscovite, and no evidence for a penetrative deformational fabric (Fig. 6A). The composition and age of this dike are similar to those of rhyolite dike samples 04-MP and 07-MP, which are strongly deformed by D3 and located a few kilometers to the southeast (see following). These field and thin section observations suggest that this dike swarm was emplaced after D2, but prior to D3 ductile extensional deformation. We suggest that the dike swarm does not have the S3 foliation because of the combination of low D3 strain at the relatively low temperatures of ~200–250 °C. At these temperatures, calcite in the marble and calc-schist country rock underwent crystal-plastic flow, but quartz in the dike did not (e.g., Burkhard, 1993; Koch et al., 1989; Ferrill et al., 2004; Passchier and Trouw, 2005), resulting in a competence contrast between the stronger rhyolite dike and the surrounding weaker marble and calc-schist.

In CL, zircons from this sample show cores with textures ranging from bright and homogeneous to oscillatory-zoned cut by newly grown oscillatory-zoned rims (Fig. 7A). Secondary ion mass spectrometry (SIMS) spots (n = 18) on rims from these zircons yield a weighted average ^{207}Pb-corrected ^{206}Pb/^{238}U age of 38.4 ± 0.5 Ma (Fig. 8A). Most zircon grains from 03-MP were composite and dominated by large cores, making microsampling for TIMS (thermal ionization mass spectrometry) analysis difficult. CL images revealed a small

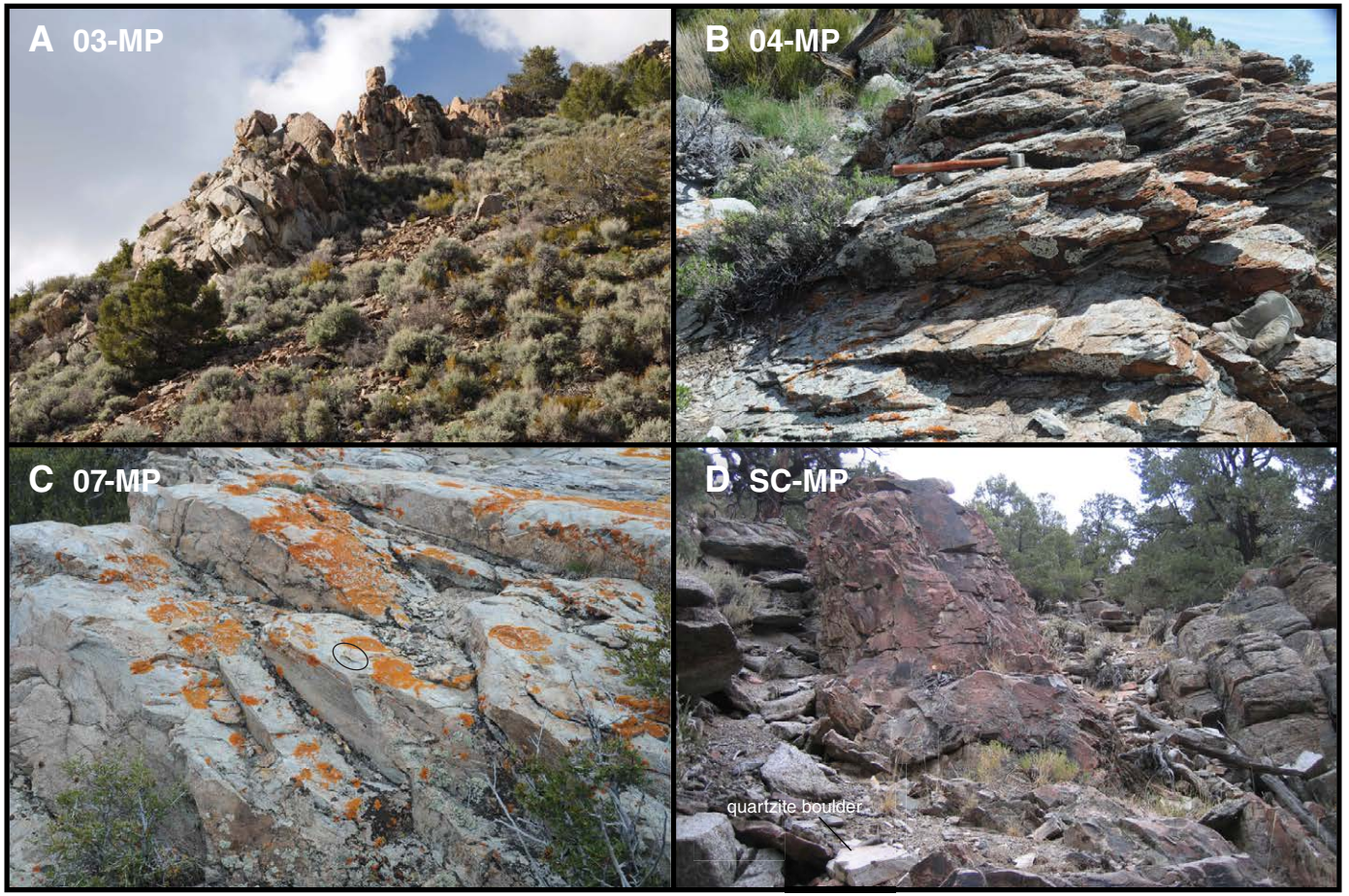

Figure 5. Field photographs of rhyolite dikes from which samples were taken for U/Pb zircon geochronology. (A) Sample 03-MP (view to northwest; pine tree in the lower right of the photograph is ~1.8 m tall). (B) Sample 04-MP (view to south; rock hammer is ~39 cm long). (C) Sample 07-MP (view to southeast; keys, which are circled, are ~6 cm long). (D) Sample SC-MP (view to north; long axis of quartzite boulder is ~65 cm). See Figure 3 for locations of samples.

subpopulation of grains without cores that were selected for high-precision analysis by CA-ID-TIMS. Based on two single grains, we calculate a weighted mean $^{206}Pb/^{238}U$ age of 37.806 ± 0.051 Ma (analytical + tracer + decay constant uncertainties) (Fig. 8B). The accuracy of the TIMS age is better than the SIMS age because the high U grains may lead to discordance in a SIMS age that is effectively removed by the chemical abrasion technique (Fig. 8D). Thus, we interpret the TIMS zircon age as a crystallization age of this dike, which is slightly older than the coexisting $^{40}Ar/^{39}Ar$ muscovite age of 37.2 ± 0.4 Ma (Lee and Sutter, 1991; age recalculated using a revised age for standard MMhb from Renne et al., 1998), suggesting that the $^{40}Ar/^{39}Ar$ age records rapid post-emplacement cooling of the dike below ~415–460 °C, the estimated closure temperature for muscovite (Kirschner et al., 1996; Harrison et al., 2009).

Samples 04-MP and 07-MP

Samples 04-MP and 07-MP were collected from fine-grained rhyolite dikes now located ~7 km southeast of sample 03-MP in the north-central part of the range (Figs. 3, 5B, and 5C). Here the dikes are exposed within strongly D3 de-

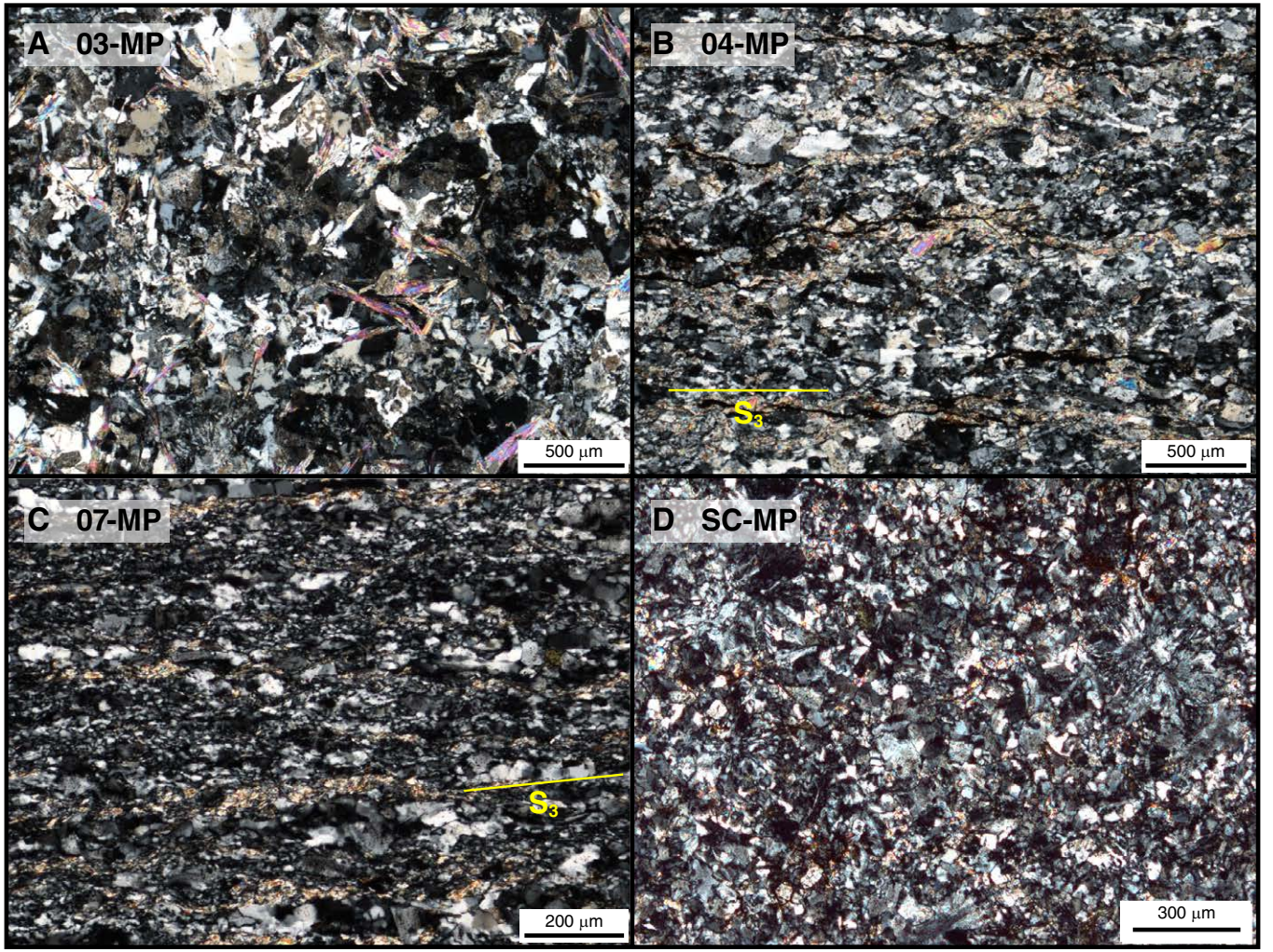

Figure 6. Photomicrographs (cross polars) of dated rhyolite dike samples. (A) Sample 03-MP. (B) Sample 04-MP. Trace of the S3 foliation is shown. (C) Sample 07-MP. Trace of the S3 foliation is shown. (D) Sample SC-MP.

formed lower plate late Cambrian to Ordovician marbles and calc-schists. In contrast to sample 03-MP, both of these dikes have a high-strain S3 foliation and associated west-northwest–east-southeast–trending mineral elongation lineation, the same as the surrounding marbles and calc-schists, indicating that these dikes were emplaced pre-D3 to syn-D3 ductile extension. In outcrop and in thin section, the strain associated with the D3 deformation is well developed, but clearly higher in sample 07-MP compared to 04-MP (cf. Figs. 5B, 5C, 6B, and 6C). In thin section, both dikes are characterized by fine-grained quartz + feldspar + muscovite, and in sample 04-MP by a well-developed foliation defined by aligned muscovite and flattened quartz, and in sample 07-MP by a mylonitic foliation defined by dynamically recrystallized quartz and flattened and strung-out muscovite (Fig. 6B, 6C). Sample 07-MP

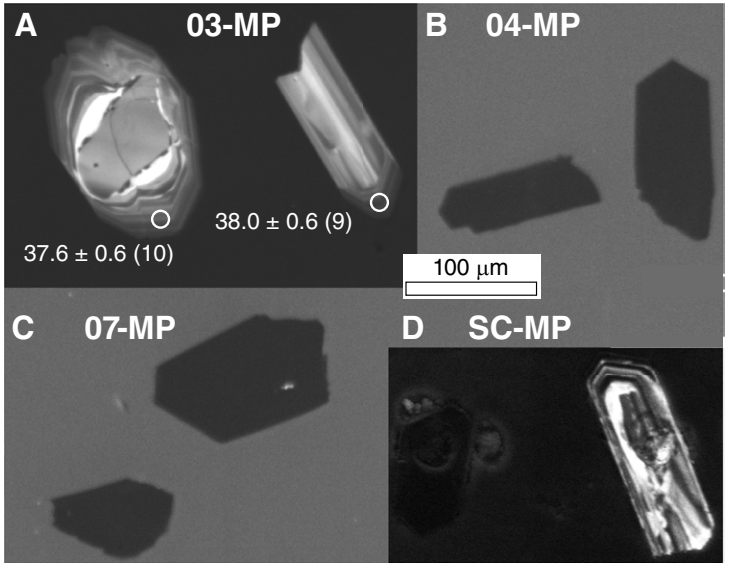

Figure 7. Representative cathodoluminescence images of zircons from rhyolite dike samples. (A) Sample 03-MP. Analyzed spots and corresponding ^{207}Pb-corrected ages (±1σ) are shown; the number in parentheses following the age corresponds to the analysis number in Table 1. (B) Sample 04-MP. (C) Sample 07-MP. (D) Sample SC-MP.

also has shear bands and a weakly developed oblique grain shape foliation in quartz; both indicate top-to-the-southeast sense of shear associated with the S3 foliation.

Zircons from both samples are uniformly black in CL (Fig. 7B, 7C), consistent with a U content of >10,000 ppm. Zircons from samples 04-MP and 07-MP analyzed by ID-TIMS yield ^{206}Pb/^{238}U ages of 37.531 ± 0.009 Ma and 37.504 ± 0.014 Ma, respectively (Fig. 8B), which we interpret as crystallization ages.

Sample SC-MP

Sample SC-MP was collected from an 80° southeast-dipping rhyolite dike within a northeast-trending dike swarm exposed north of a septum of Proterozoic McCoy Creek Group rocks sandwiched within the Jurassic Old Mans tonalite located in the Silver Creek area, southern part of the northern Snake Range (Figs. 3 and 5D). Here the Silver Creek dike swarm cuts across the D3 mylonitically deformed Old Mans tonalite (Miller et al., 1999b), and thus was emplaced after D3 ductile extensional deformation had ceased. The undeformed nature of the dike is confirmed in thin section, which exhibits delicate intergrowths of quartz + feldspar + muscovite with lesser biotite, radiating clusters of quartz and feldspar, and no evidence for crystal plastic deformation (Fig. 6D).

Zircons from this sample display a range of uniformly black, high U content grains, and oscillatory-zoned grains in CL. The U/Pb analyses were trimmed by excluding grains with ^{207}Pb/^{235}U errors >10%, and by using the TuffZirc algorithm of Ludwig (2003) to statistically eliminate young and old analyses affected by Pb loss and inheritance, respectively. After this trimming, 25 of 40 total analyses yield a ^{206}Pb/^{238}U weighted average age of 22.49 ± 0.36 Ma (2σ analytical + 2σ systematic uncertainty) (Fig. 8C). We interpret this age to date the timing of crystallization of the rhyolite dike, and the undeformed nature of the dike thus indicates that ductile extensional deformation in the lower plate had ceased at this location by this time.

Interpretation of Zircon and Published Thermochronologic Ages

Our new ^{238}U-^{206}Pb zircon ages, combined with new and published field, petrographic, and structural observations, indicate that the high-strain D3 middle crustal ductile extensional deformation, characterized by ~15.6–18.2 km of horizontal ductile extensional deformation across the southern part of the northern Snake Range, initiated sometime after ca. 37.8 Ma and ceased on the southern end of the range by ca. 22.5 Ma (Fig. 8). These age constraints suggest that D3 ductile extensional deformation may have been prolonged, lasting as long as 15.3 m.y. However, thermochronologic data suggest that cessation of ductile deformation was not synchronous across the range. Contours of muscovite K-Ar and ^{40}Ar/^{39}Ar total gas ages from the early Cambrian Prospect Mountain Quartzite and Pioche Shale show a systematic decrease in age from west to east across the range (Fig. 3) (Lee and Sutter, 1991), and calculated lower plate cooling histories derived from MDD analyses of ^{40}Ar/^{39}Ar potassium feldspar data (Lee, 1995), muscovite ^{40}Ar/^{39}Ar ages (Lee and Sutter, 1991), and apatite fission track ages (Miller et al., 1999a) suggest as many as three periods of rapid cooling in the lower plate; middle Eocene and middle Oligocene on the northwestern flank of the range, and early to middle Miocene across the central and eastern parts of the range (Fig. 9). These cooling histories imply asymmetric exhumation (unroofing) and consequent differential cooling as lower plate rocks on the western flank of the range were exhumed into the brittle field and cooled before the lower plate rocks in the central and the eastern parts of the range (Lee, 1995) (Fig. 9). The middle Eocene cooling (exhumation) episode on the northwestern flank of the range, recorded in potassium feldspar samples KPA5 and KPA4 collected from a pegmatite and aplite dike swarm (Lee, 1995) (Fig. 3), occurred at temperatures of ≤300 °C and >300 °C, respectively, just below and above the estimated minimum temperature required for crystal plastic flow in wet quartz (e.g., Koch et al., 1989). Undeformed sample KPA5 is located outside the zone of ductile extensional deformation, whereas moderately penetratively D3 deformed sample KPA4 is located within that zone. This apparent cooling episode is older than our new maximum age constraint on the timing of ductile extension, and thus may be the result of: (1) conductive cooling following emplacement of the dike swarm during the early to middle Eocene (Lee and Sutter, 1991); (2) a period of minor

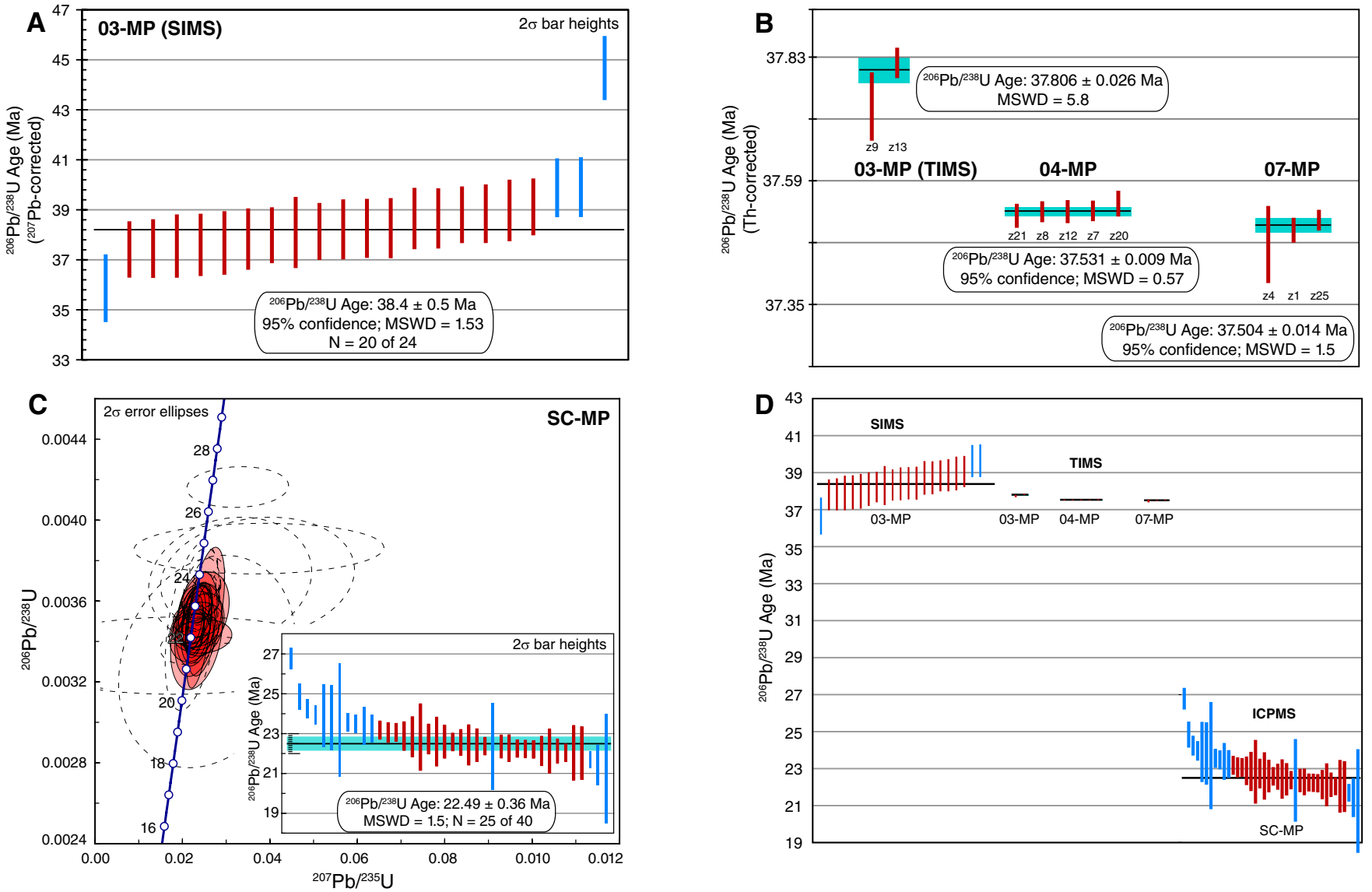

Figure 8. Interpretative plots of rhyolite dike zircon data. (A) Weighted average of ^{207}Pb-corrected secondary ion mass spectrometry (SIMS) ages (±95% confidence, with error in the standard) from sample 03-MP. Note that two sets of two spots yielded the same age ± error; 2 spots yielded ages of 37.5 ± 0.6 Ma and 2 spots yielded ages of 39.9 ± 0.6 Ma. MSWD—mean square of weighted deviates. (B) Weighted average of chemical abrasion–thermal ionization mass spectrometry (CA-TIMS) generated Th-corrected ages from samples 03-MP, 04-MP, and 07-MP. Reported error is analytical uncertainty. (C) Concordia plot of data from sample SC-MP. Reported error is 2σ analytical and systematic uncertainty. (D) Compilation of ^{206}Pb/^{238}U ages from SIMS, TIMS, and inductively coupled plasma–mass spectrometry (ICP-MS) analyses for samples 03-MP, 04-MP, 07-MP, and SC-MP. Red and blue vertical bars (included and excluded, respectively, in the calculation of average age) correspond to red and blue vertical bars in A–C. Black horizontal line is the weighted average age for each set of analyses; for the TIMS analyses the weighted average line is thicker than the error associated with each analysis.

TABLE 1. U-Pb ISOTOPIC DATA FROM SAMPLE 03-MP COLLECTED BY SHRIMP-RG

Number	Spot name	U (ppm)	Pb (ppm)	Th/U	f_{206} (%)	$^{207}Pb/^{206}Pb$ uncorrected	% error	$^{206}Pb/^{238}U$ uncorrected	Error (%)	$^{206}Pb/^{238}U$ corrected	Error (%)	$^{206}Pb/^{238}U$ age (Ma) 204 corrected	1σ	$^{206}Pb/^{238}U$ age (Ma) 208 corrected	1σ	$^{206}Pb/^{238}U$ age (Ma) 207 corrected	1σ
1	03MP-1.1	748	245	0.34	12.81	0.148	5.7	0.010	5.4	0.006	1.4	35.9	0.8	36.0	0.7	35.9	0.7
2	03MP-11.1	759	207	0.28	0.47	0.050	4.1	0.010	3.8	0.006	1.5	37.4	0.6	37.5	0.6	37.4	0.6
3	03MP-22.1	757	202	0.28	0.36	0.050	3.9	0.011	2.3	0.006	1.5	37.9	0.6	37.4	0.6	37.5	0.6
4	03MP-19.1	506	117	0.24	–0.02	0.047	4.4	0.010	4.0	0.006	1.7	37.3	0.6	37.3	0.7	37.5	0.6
5	03MP-10.1	543	120	0.23	–0.20	0.045	5.1	0.010	2.6	0.006	1.6	36.8	0.7	37.4	0.6	37.6	0.6
6	03MP-7.1	556	124	0.23	0.44	0.050	5.1	0.010	4.0	0.006	1.7	37.9	0.6	37.3	0.7	37.7	0.6
7	03MP-16.1	806	215	0.28	0.30	0.049	3.5	0.010	3.6	0.006	1.6	37.8	0.6	37.8	0.6	37.8	0.6
8	03MP-9.1	858	187	0.23	0.49	0.051	4.0	0.011	4.8	0.006	1.4	38.0	0.6	38.1	0.6	38.0	0.6
9	03MP-13.1	361	66	0.19	–0.29	0.044	5.3	0.010	3.4	0.006	1.8	38.1	0.7	37.8	0.7	38.1	0.7
10	03MP-14.1	775	208	0.28	0.49	0.051	3.3	0.011	3.6	0.006	1.5	38.2	0.6	38.1	0.6	38.1	0.6
11	03MP-21.1	729	172	0.24	–0.41	0.044	4.0	0.011	3.1	0.006	1.6	37.7	0.6	38.0	0.6	38.2	0.6
12	03MP-20.1	669	143	0.22	0.04	0.047	4.4	0.011	4.0	0.006	1.5	38.3	0.6	38.2	0.6	38.3	0.6
13	03MP-31.1	895	157	0.18	0.65	0.052	3.7	0.011	1.6	0.006	1.6	38.3	0.6	38.4	0.6	38.3	0.6
14	03MP-4.1	675	145	0.22	0.20	0.048	4.6	0.010	3.0	0.006	1.6	38.4	0.6	38.6	0.6	38.7	0.6
15	03MP-6.1	662	154	0.24	0.41	0.050	4.5	0.010	4.8	0.006	1.5	38.4	0.6	38.5	0.6	38.7	0.6
16	03MP-15.1	838	214	0.26	0.07	0.047	3.3	0.010	4.8	0.006	1.4	38.3	0.6	38.6	0.6	38.8	0.6
17	03MP-8.1	783	178	0.23	0.08	0.047	4.5	0.010	3.4	0.006	1.5	38.7	0.6	38.8	0.6	38.8	0.6
18	03MP-5.1	642	136	0.22	–0.38	0.044	4.7	0.010	3.8	0.006	1.6	38.7	0.6	38.5	0.6	39.0	0.6
19	03MP-17.1	886	194	0.23	0.07	0.047	3.4	0.011	3.6	0.006	1.4	38.9	0.6	39.1	0.6	39.1	0.6
20	03MP-12.1	832	211	0.26	–0.11	0.046	4.1	0.011	3.8	0.006	1.5	39.7	0.6	39.8	0.6	39.9	0.6
21	03MP-18.1	768	182	0.24	0.13	0.048	5.1	0.011	3.6	0.006	1.5	39.9	0.6	40.0	0.6	39.9	0.6
22	03MP-2.1	804	169	0.22	0.16	0.048	4.2	0.012	3.1	0.007	1.4	44.7	0.6	44.9	0.7	44.7	0.6

Note: SHRIMP-RG—sensitive high-resolution ion microprobe–reverse geometry; f_{206}—fraction of total ^{206}Pb that is common ^{206}Pb. Weighted mean 207-corrected $^{206}Pb/^{238}U$ age (±95% confidence, with error in standard) of numbers 2–21 is 38.4 ± 0.5 Ma.

exhumation prior to the onset age for ductile extension, which may be as old as ca. 37.8 Ma based on our zircon ages and field, petrologic, and structural observations; or (3) little or no middle Eocene cooling if the error associated with the cooling curves is taken into account (Fig. 9). The MDD cooling curves, combined with apatite fission track ages, indicate that the cooling episode during the early to middle Miocene initiated at temperatures of ~300–350 °C in the central and eastern parts of the range, and reached temperatures of ~100 °C uniformly across the range by the middle Miocene (Lee, 1995; Miller et al., 1999a) (Fig. 9). These data, combined with our zircon ages, imply that during the latest Oligocene–earliest Miocene the lower plate underwent either the major phase of ductile extension or the waning stages of ductile extension during the earliest stages of a major phase of upper crustal normal faulting (see Discussion for details).

Gébelin et al. (2014) inferred that muscovite $^{40}Ar/^{39}Ar$ total gas ages of ca. 49–45 Ma from strongly disturbed age spectra observed in the Prospect Mountain Quartzite in Negro Creek on the west flank of the range recorded the time of formation of the subhorizontal mylonitic foliation, west-northwest–east-southeast stretching lineation, microstructures, and c-axis fabrics observed there (Lee et al., 1987) (Fig. 3). If true, this interpretation implies that ductile extensional deformation was ongoing in the lower plate during the early to middle Eocene exhumation episode and before the maximum age for the timing of ductile extension provided by our new zircon U/Pb ages. We suggest that these strongly disturbed $^{40}Ar/^{39}Ar$ age spectra record geologically meaningless ages and are the result of any combination of the following: (1) diffusive loss of argon in muscovites that resided in the partial retention zone or during a thermal excursion resulting in partial outgassing of muscovite (e.g., Baldwin and Lister, 1998; Little et al., 1999; Harrison and Zeitler, 2005); (2) muscovite that underwent at least two deformation and/or neorecrystallization events (i.e., Cretaceous and Paleogene–Neogene) resulting in samples containing at least two age populations of muscovite (e.g., Wijbrans and McDougall, 1986; Beltrando et al., 2009; Kula et al., 2010); (3) a mix of coarse older grains (mica fish that record the kinematics of D3 deformation; Lee et al., 1987; Gébelin et al., 2014) and fine neocrystallized grains (fine-grained recrystallized muscovite along fish rims and tails and in pressure shadows) (Lee et al., 1987; Gébelin et al., 2014) that underwent a heterogeneous thermal overprint leading to internal age gradients (e.g., Kula et al., 2010); and/or as shown with igneous muscovites whereby grain size positively correlates with $^{40}Ar/^{39}Ar$ age (Kula and Spell, 2012), (4) these metamorphic samples with different muscovite grain sizes (coarse-grained mica fish versus fine-grained muscovite) may record more than one thermal history resulting in the observed age gradients.

TABLE 2. U-Pb ISOTOPIC DATA COLLECTED BY THERMAL IONIZATION MASS SPECTROMETRY

Zircon fraction	Dates (Ma)								Composition				Isotopic ratios						
	$^{206}Pb/^{238}U$ <Th>[a]	±2σ abs.	$^{207}Pb/^{235}U$[b]	±2σ abs.	$^{207}Pb/^{206}Pb$[b]	±2σ abs.	Correlation coefficient	Disc.[c] (%)	Th/U[d]	Pb* (pg)[e]	Pb[c] (pg)[f]	Pb*/ Pbc[g]	$^{206}Pb/^{204}Pb$[h]	$^{206}Pb/^{238}U$[i]	±2σ (%)	$^{207}Pb/^{235}U$[h]	±2σ (%)	$^{207}Pb/^{206}Pb$[h]	±2σ (%)
Sample 03-MP																			
z9	37.734	0.064	37.831	0.491	50.0	27	1.071	24.68	0.51	5.70	0.39	15	898	0.0058559	0.171	0.037960	1.323	0.047036	1.14
z13	37.819	0.028	38.158	0.287	66.0	18	0.043	42.88	0.23	6.28	0.31	20	1311	0.0058679	0.074	0.038295	0.766	0.047354	0.766
Weighted mean $^{206}Pb/^{238}U$ age (± analytical uncertainty; analytical + tracer uncertainties; analytical + tracer + decay constant uncertainties): 37.806 ± 0.026; 0.031; 0.051 Ma																			
Sample 04-MP																			
z7	37.532	0.018	37.629	0.035	50.4	1.3	0.882071	25.66	0.26	123	0.26	471	30212	0.0058233	0.048	0.037755	0.094	0.047043	0.054
z8	37.530	0.018	37.642	0.024	51.3	2.1	–0.150194	26.98	0.27	62.9	0.29	214	13687	0.0058231	0.049	0.037768	0.066	0.047061	0.087
z12	37.530	0.020	37.620	0.036	49.8	1.4	0.861815	24.88	0.29	214	0.34	630	40159	0.0058231	0.055	0.037745	0.098	0.047033	0.056
z20	37.546	0.023	37.681	0.049	52.7	2.2	0.762785	28.98	0.29	83.6	0.36	230	14683	0.0058256	0.062	0.037807	0.132	0.047090	0.093
z21	37.522	0.021	37.615	0.130	50.1	8.0	0.381024	25.32	0.24	15.6	0.32	49	3162	0.0058217	0.057	0.037740	0.352	0.047038	0.335
Weighted mean $^{206}Pb/^{238}U$ age (± analytical uncertainty; analytical + tracer uncertainties; analytical + tracer + decay constant uncertainties): 37.5314 ± 0.0090; 0.019; 0.044 Ma																			
Sample 07-MP																			
z1	37.494	0.022	37.444	0.142	40.8	8.5	0.544390	8.40	0.23	19.6	0.36	54	3499	0.0058172	0.060	0.037565	0.386	0.046856	0.357
z4	37.466	0.073	37.402	0.966	39.8	62	0.260989	6.13	0.24	1.45	0.24	6	402	0.0058130	0.196	0.037522	2.630	0.046836	2.59
z25	37.513	0.018	37.576	0.064	48.1	3.5	0.643061	22.18	0.25	37.2	0.29	126	8161	0.0058203	0.049	0.037700	0.172	0.046998	0.145
Weighted mean $^{206}Pb/^{238}U$ age (± analytical uncertainty; analytical + tracer uncertainties; analytical + tracer + decay constant uncertainties): 37.504 ± 0.014; 0.022; 0.045 Ma																			

Note: abs.—absolute; Disc.—discordance.
[a]Corrected for initial Th/U disequilibrium using radiogenic ^{208}Pb and Th/U(magma) = 4.00000.
[b]Isotopic dates calculated using the decay constants $\lambda^{238}U$ = 1.55125E-10 and $\lambda^{235}U$ = 9.8485E-10 (Jaffey et al., 1971).
[c]Discordance = 100 – [100($^{206}Pb/^{238}U$ date)/($^{207}Pb/^{206}Pb$ date)].
[d]Th contents calculated from radiogenic ^{208}Pb and the $^{207}Pb/^{206}Pb$ date of the sample, assuming concordance between U-Th and Pb systems.
[e]Total mass of radiogenic Pb.
[f]Total mass of common Pb.
[g]Ratio of radiogenic Pb (including ^{208}Pb) to common Pb.
[h]Measured ratio corrected for fractionation and spike contribution only.
[i]Measured ratios corrected for fractionation, tracer, and blank.

Our constraints on the timing of D3 mid-crustal ductile extensional deformation overlap with those based on other thermochronological data (cf. Lee and Sutter, 1991; Miller et al., 1999a; Gébelin et al., 2011). Lee and Sutter (1991) argued that ductile extension occurred between ca. 37.2 Ma, the muscovite $^{40}Ar/^{39}Ar$ plateau age from one of the vertical, undeformed dikes from the Northern dike swarm on the northwest side of the range, and ca. 24.5 Ma, muscovite $^{40}Ar/^{39}Ar$ plateau or near plateau ages from metasedimentary rocks on the eastern flank of the range (Lee et al., 1987; age recalculated based on the procedures of Renne et al., 1998); combined with microstructural studies and quartz petrofabrics, this suggested that ductile extensional deformation ceased at this time or soon thereafter. Similarly, Gébelin et al. (2011) used a ca. 23 Ma muscovite $^{40}Ar/^{39}Ar$ plateau age on the east flank of the range, combined with microstructural, quartz petrofabric, and stable isotopic investigations, to suggest that ductile extension along the east flank of the range ceased by this time. Gébelin et al. (2011) also argued that muscovite $^{40}Ar/^{39}Ar$ ages indicated that mylonitic ductile extensional deformation along the eastern flank of the range occurred over a time span of ca. 27–23 Ma. Although this time period overlaps with the bounds placed on the timing of ductile extension our zircon ages provide, with the exception of the ca. 23 Ma muscovite $^{40}Ar/^{39}Ar$ plateau age, the muscovite samples reported in Gébelin et al. (2011) yielded strongly disturbed $^{40}Ar/^{39}Ar$ age spectra. As we argue here, these disturbed spectra are likely the result of any combination of processes (e.g., diffusive argon loss, a mix of old and new grains), and thus the ages are likely geologically meaningless. Many of the mica $^{40}Ar/^{39}Ar$ samples reported in Lee and Sutter (1991) also exhibit strongly disturbed age spectra, indicating that these ages are also geologically meaningless.

Our ca. 22.5 Ma age on the post-D3 dike requires a reinterpretation of the significance of fission track results for the timing of ductile extensional deformation (Miller et al., 1999a). Based on apatite and zircon (22 and 3 samples, respectively) fission track ages from across the lower plate, Miller et al. (1999a) argued that extensional mylonitization could be as young as ca. 17 Ma (the mean age, within error, of all apatite and zircon fission track samples), younger

TABLE 3. U-Pb ISOTOPE DATA FROM SAMPLE SC-MP COLLECTED BY LA-MC-ICP-MS

				Isotope ratios[a]							Apparent ages[a] (Ma)							
Analysis[b]	U (ppm)	$^{206}Pb/^{204}Pb$	U/Th	$^{206}Pb^*/^{207}Pb^*$	±1σ (%)	$^{207}Pb^*/^{235}U$	±1σ (%)	$^{206}Pb^*/^{238}U$	±1σ (%)	Err.[c] cor.	$^{206}Pb^*/^{238}U$	±1σ[d]	$^{206}Pb^*/^{238}U$	±1σ[d]	$^{207}Pb^*/^{235}U$	±1σ[d]	Best age	±1σ[d]
1[e]	8129	5688	2.7	19.3887	6.0	0.0252	7.0	0.0035	3.7	0.53	22.8	0.8	25.3	1.8	266.7	137.2	22.8	0.8
2[f]	9124	6626	3.1	20.6674	6.8	0.0241	7.0	0.0036	1.5	0.22	23.2	0.4	24.2	1.7	118.1	161.2	23.2	0.4
3[e]	9993	5410	2.5	20.4083	4.6	0.0240	4.9	0.0036	1.6	0.33	22.9	0.4	24.1	1.2	147.8	107.9	22.9	0.4
4[f]	8866	6908	2.6	19.6147	5.5	0.0262	5.6	0.0037	1.0	0.18	24.0	0.2	26.2	1.4	240.0	126.4	24.0	0.2
5[e]	22305	11980	2.6	20.8743	7.9	0.0232	8.4	0.0035	2.7	0.33	22.6	0.6	23.3	1.9	94.6	188.1	22.6	0.6
6[g]	1148	694	0.8	13.7742	24.2	0.0372	24.4	0.0037	3.3	0.14	23.9	0.8	37.1	8.9	1002.8	498.4	23.9	0.8
7[e]	6922	5328	3.5	20.6060	7.4	0.0241	7.4	0.0036	1.0	0.13	23.2	0.2	24.2	1.8	125.1	173.4	23.2	0.2
8[g]	11575	3300	1.8	17.6258	14.6	0.0326	14.6	0.0042	1.0	0.07	26.8	0.3	32.6	4.7	481.2	324.2	26.8	0.3
9[g]	10522	2138	1.3	14.2105	31.2	0.0375	31.2	0.0039	1.3	0.04	24.8	0.3	37.3	11.5	939.2	655.4	24.8	0.3
10[f]	8166	7338	4.0	20.2192	4.5	0.0249	4.6	0.0036	1.0	0.22	23.5	0.2	24.9	1.1	169.6	105.6	23.5	0.2
11[e]	7559	6046	3.5	20.3257	10.0	0.0232	10.5	0.0034	3.1	0.30	22.0	0.7	23.3	2.4	157.3	233.8	22.0	0.7
12[g]	705	1042	1.9	16.0262	105.7	0.0317	105.9	0.0037	6.1	0.06	23.7	1.4	31.7	33.0	687.8	562.4	23.7	1.4
13[e]	7329	4662	4.0	19.7137	9.3	0.0248	9.5	0.0035	2.2	0.23	22.8	0.5	24.9	2.3	228.4	214.9	22.8	0.5
14[g]	2887	2282	2.9	17.7725	31.6	0.0256	32.3	0.0033	6.5	0.20	21.2	1.4	25.7	8.2	462.9	716.5	21.2	1.4
15[e]	12489	9488	2.9	20.6171	3.9	0.0236	4.2	0.0035	1.7	0.39	22.7	0.4	23.7	1.0	123.9	92.0	22.7	0.4
16[e]	7909	7598	4.3	20.7935	9.6	0.0229	9.7	0.0035	1.0	0.10	22.2	0.2	23.0	2.2	103.8	228.5	22.2	0.2
17[e]	24987	16454	2.8	21.0061	5.5	0.0235	5.6	0.0036	1.1	0.19	23.1	0.2	23.6	1.3	79.7	131.7	23.1	0.2
18[e]	22651	12652	2.7	20.5906	9.7	0.0235	9.8	0.0035	1.0	0.10	22.6	0.2	23.6	2.3	126.9	229.3	22.6	0.2
19[e]	8736	7270	3.2	21.2980	3.2	0.0227	3.5	0.0035	1.5	0.41	22.6	0.3	22.8	0.8	46.8	76.4	22.6	0.3
20[e]	26370	17094	2.5	20.8036	3.7	0.0228	4.0	0.0034	1.4	0.35	22.1	0.3	22.9	0.9	102.6	87.6	22.1	0.3
21[e]	9030	6544	5.0	21.5044	9.3	0.0220	9.4	0.0034	1.7	0.18	22.1	0.4	22.1	2.1	23.7	222.9	22.1	0.4
22[e]	13041	4516	2.1	19.8579	3.8	0.0238	4.9	0.0034	3.0	0.62	22.0	0.7	23.8	1.1	211.5	88.4	22.0	0.7
23[e]	7570	5076	2.9	20.7143	5.8	0.0232	6.2	0.0035	2.3	0.37	22.4	0.5	23.3	1.4	112.8	135.9	22.4	0.5
24[g]	2004	2230	2.7	16.5372	24.4	0.0309	24.7	0.0037	3.5	0.14	23.8	0.8	30.9	7.5	620.4	534.8	23.8	0.8
25[e]	9384	5138	1.8	20.7341	4.7	0.0238	4.8	0.0036	1.0	0.21	23.1	0.2	23.9	1.1	110.5	111.3	23.1	0.2
26[f]	8808	7832	4.1	22.1391	11.9	0.0210	12.0	0.0034	1.0	0.08	21.7	0.2	21.1	2.5	–46.6	291.3	21.7	0.2
27[g]	1283	1498	1.2	23.6061	80.0	0.0194	80.0	0.0033	2.4	0.03	21.4	0.5	19.5	15.5	–205.0	2448.3	21.4	0.5
28[f]	12761	9580	3.3	20.6318	6.9	0.0243	7.2	0.0036	2.0	0.28	23.4	0.5	24.4	1.7	122.2	162.9	23.4	0.5
29[e]	15240	6058	2.9	19.4589	7.8	0.0247	8.0	0.0035	1.9	0.23	22.4	0.4	24.8	2.0	258.4	179.5	22.4	0.4
30[e]	11176	8322	2.7	20.7635	7.8	0.0228	8.2	0.0034	2.5	0.31	22.1	0.6	22.9	1.9	107.2	185.0	22.1	0.6
31[e]	12732	10610	4.1	21.6435	7.7	0.0221	7.8	0.0035	1.0	0.13	22.4	0.2	22.2	1.7	8.2	186.3	22.4	0.2
32[e]	9063	9714	4.3	21.1517	6.7	0.0225	6.8	0.0034	1.0	0.15	22.2	0.2	22.6	1.5	63.2	159.9	22.2	0.2
33[f]	17997	15798	3.7	21.5488	10.3	0.0222	11.4	0.0035	4.9	0.43	22.4	1.1	22.3	2.5	18.8	246.8	22.4	1.1
34[e]	15218	13182	3.8	21.3603	4.2	0.0224	4.4	0.0035	1.3	0.30	22.3	0.3	22.5	1.0	39.8	99.3	22.3	0.3
35[e]	25142	12666	2.1	21.4782	4.6	0.0225	5.0	0.0035	1.9	0.37	22.6	0.4	22.6	1.1	26.6	111.2	22.6	0.4
36[e]	25182	15708	2.0	20.9067	3.8	0.0228	4.1	0.0035	1.5	0.37	22.3	0.3	22.9	0.9	90.9	89.7	22.3	0.3
37[e]	6251	4648	3.3	19.1427	10.8	0.0247	10.9	0.0034	1.0	0.09	22.0	0.2	24.7	2.7	295.9	247.4	22.0	0.2
38[f]	21354	14574	2.9	20.9231	5.2	0.0248	5.3	0.0038	1.0	0.19	24.2	0.2	24.9	1.3	89.1	122.6	24.2	0.2
39[f]	9188	5324	1.8	19.7505	5.0	0.0256	5.1	0.0037	1.0	0.20	23.6	0.2	25.6	1.3	224.1	114.7	23.6	0.2
40[e]	9945	7142	3.1	20.9482	6.3	0.0227	6.4	0.0035	1.0	0.16	22.2	0.2	22.8	1.4	86.2	150.5	22.2	0.2

Note: LA-MC-ICP-MS—laser ablation–multicollector–inductively coupled plasma–mass spectrometer.
[a]U decay constants and composition: $^{238}U = 9.8485 \times 10^{-10}$, $^{235}U = 1.55125 \times 10^{-10}$, $^{238}U/^{235}U = 137.88$.
[b]Analysis refers to the LA-ICP-MS analysis locations in the order in which they were analyzed.
[c]Err. Cor. refers to the correlation of errors between $^{207}Pb/^{235}U$ and $^{206}Pb/^{238}U$.
[d]Apparent age errors are analytical only and do not include systematic errors. The 2σ systematic standard error accumulated during this analysis session was 1.5%.
[e]Analysis used to calculate the $^{206}Pb/^{238}U$ weighted average age for sample SC-MP.
[f]Analysis omitted from the $^{206}Pb/^{238}U$ weighted average age for sample SC-MP based on the TuffZirc statistical algorithm of Ludwig (2003).
[g]Analysis omitted from the $^{206}Pb/^{238}U$ weighted average age for sample SC-MP due to large $^{207}Pb/^{235}U$ errors.

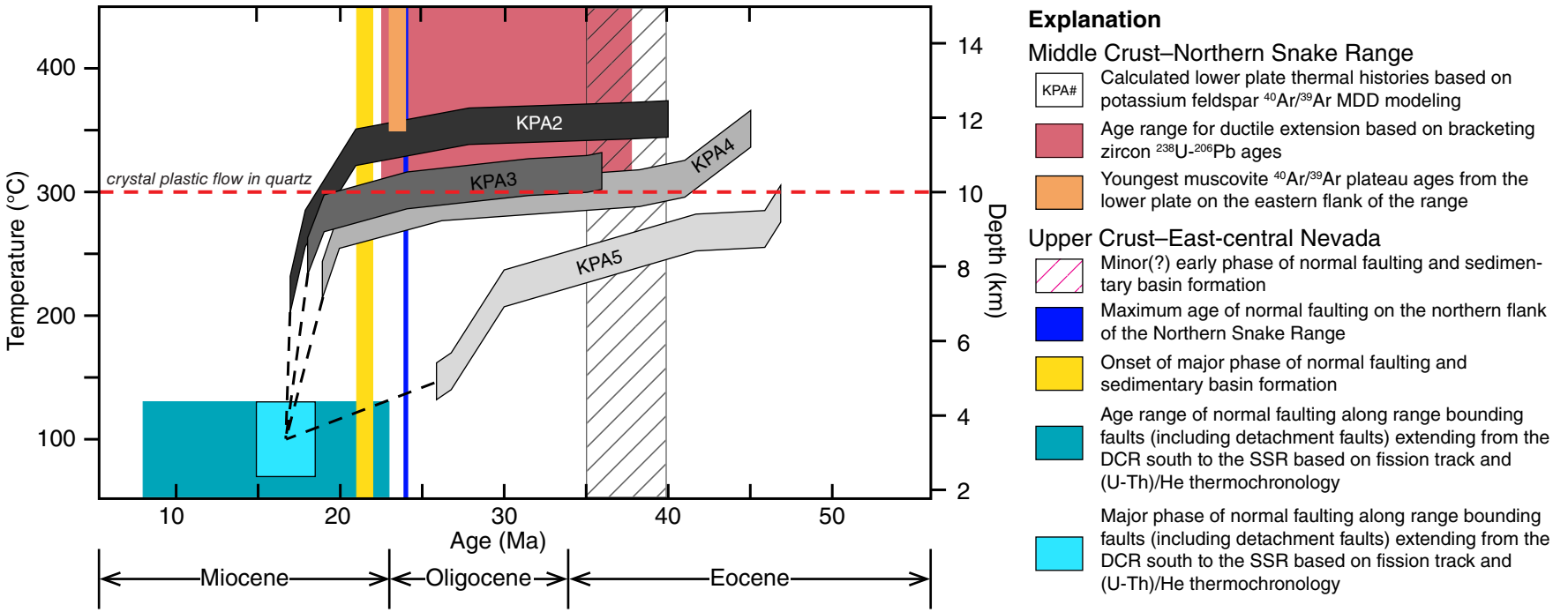

Figure 9. Compilation of geochronologic-thermochronologic data as a function of temperature-depth for the lower plate of the northern Snake Range, and age of normal faulting in the upper crust. Depth estimate is based on a 30 °C/km geothermal gradient; dashed red line indicates the minimum temperature at which wet quartz will be likely to deform crystal plastically (Koch et al., 1989). Data sources from the lower plate: dike zircon U/Pb age brackets on ductile extension are from this study; muscovite $^{40}Ar/^{39}Ar$ ages are from Lee and Sutter (1991) and Gébelin et al. (2011); potassium feldspar $^{40}Ar/^{39}Ar$ multiple diffusion domain (MDD) cooling histories (shades of gray for samples KPA2, KPA3, KPA4, and KPA5 collected from a pegmatite and aplite dike swarm; cooling curve swaths incorporate estimated error in cooling histories; see Fig. 3 for location) are from Lee (1995); mean apatite fission track age is from Miller et al. (1999a). Data sources from the upper plate: major and minor(?) phases of normal faulting and sedimentary basin formation, east-central Nevada, are from Miller et al. (1999a) and Ruksznis (2015); maximum age of normal faulting on the northern flank of the northern Snake Range is from Gans et al. (1989); fission track and (U-Th)/He data are from Miller et al. (1999a), Metcalf (2006), and Evans et al. (2015). DCR—Deep Creek Range; SSR—southern Snake Range. See text for discussion.

than any other constraints. In this interpretation, the lower plate cooled (was exhumed) from >310 °C (estimated closure temperature, T_c, for zircon fission tracks), a temperature at which wet quartz may undergo crystal plastic flow (Koch et al., 1989), to <100 °C (estimated T_c for apatite fission tracks), a temperature well within the brittle field, at ca. 17 Ma. The 310 °C T_c for zircon fission track (Tagami and Dumitru, 1996) cited in Miller et al. (1999a) was based on laboratory studies and is higher compared to a rapid cooling rate T_c of ~260–265 °C based on field studies (e.g., Foster et al., 1996; Brandon and Vance, 1992). The damage-free zircons in laboratory studies versus the radiated damaged natural zircons in field-based studies may explain the higher estimated T_c in the former versus the lower estimated T_c in the latter (Rahn et al., 2004). Thus, we argue that the zircon ca. 17 Ma fission track age more likely reflects cooling below ~260–265 °C, a temperature below the ~300 °C minimum temperature needed for crystal plastic flow in quartz (e.g., Koch et al., 1989), and therefore our U/Pb zircon age of ca. 22.5 Ma provides a minimum age for ductile extensional deformation.

In summary, our new U/Pb zircon ages combined with published potassium feldspar MDD modeling, muscovite $^{40}Ar/^{39}Ar$ plateau ages, and zircon and apatite fission track ages from the lower plate of the northern Snake Range (Lee and Sutter, 1991; Lee, 1995; Miller et al., 1999a; Gébelin et al., 2011) (Fig. 9) indicate that lower plate ductile extensional deformation is bracketed between ca. 37.8 and ca. 22.5 Ma, but was diachronous across the range. Thus, the northern Snake Range lower plate may record an episodic ductile extensional strain history between the late Eocene and latest Oligocene–earliest Miocene, although we do not know how many deformation episodes occurred or the duration of each episode. For example, we pose here (see Discussion) a speculative and permissible episodic deformational scenario whereby 30%–40% of the total horizontal ductile extension in the lower plate occurred during

the late Eocene and 60%–70% of the total occurred in the latest Oligocene–earliest Miocene. Alternatively, the lower plate may record a single, protracted ductile extensional strain history between the late Eocene and latest Oligocene–earliest Miocene. In this interpretation, the period of slow cooling in the lower plate indicated by the potassium feldspar MDD cooling curves between the late Eocene and early Miocene suggests ductile shear in a subhorizontal or low-angle shear zone, and the episode of rapid cooling that began in the early Miocene indicates exhumation within a moderately to steeply east-dipping, top-to-the-east ductile shear zone that transitions, updip, into the footwall of the brittle NSRD (Lee, 1995; Miller et al., 1999a) (Figs. 9 and 10).

DISCUSSION

The 2D and 3D analogue models make predictions about the key factors in the genesis of core complexes; viscosity in the lower plate, formation of the detachment fault, and a close spatial-temporal relationship between deformation in the upper plate, lower plate, and detachment fault. These models showed that decreased viscosity in the lower plate is critical to the formation of metamorphic core complexes. Convective flow of meteoric fluids within hot (~400 °C) quartz-dominated lower plate rocks of the northern Snake Range (Lee et al., 1987; Lee, 1995; Gébelin et al., 2011, 2014) sufficiently reduced vis-

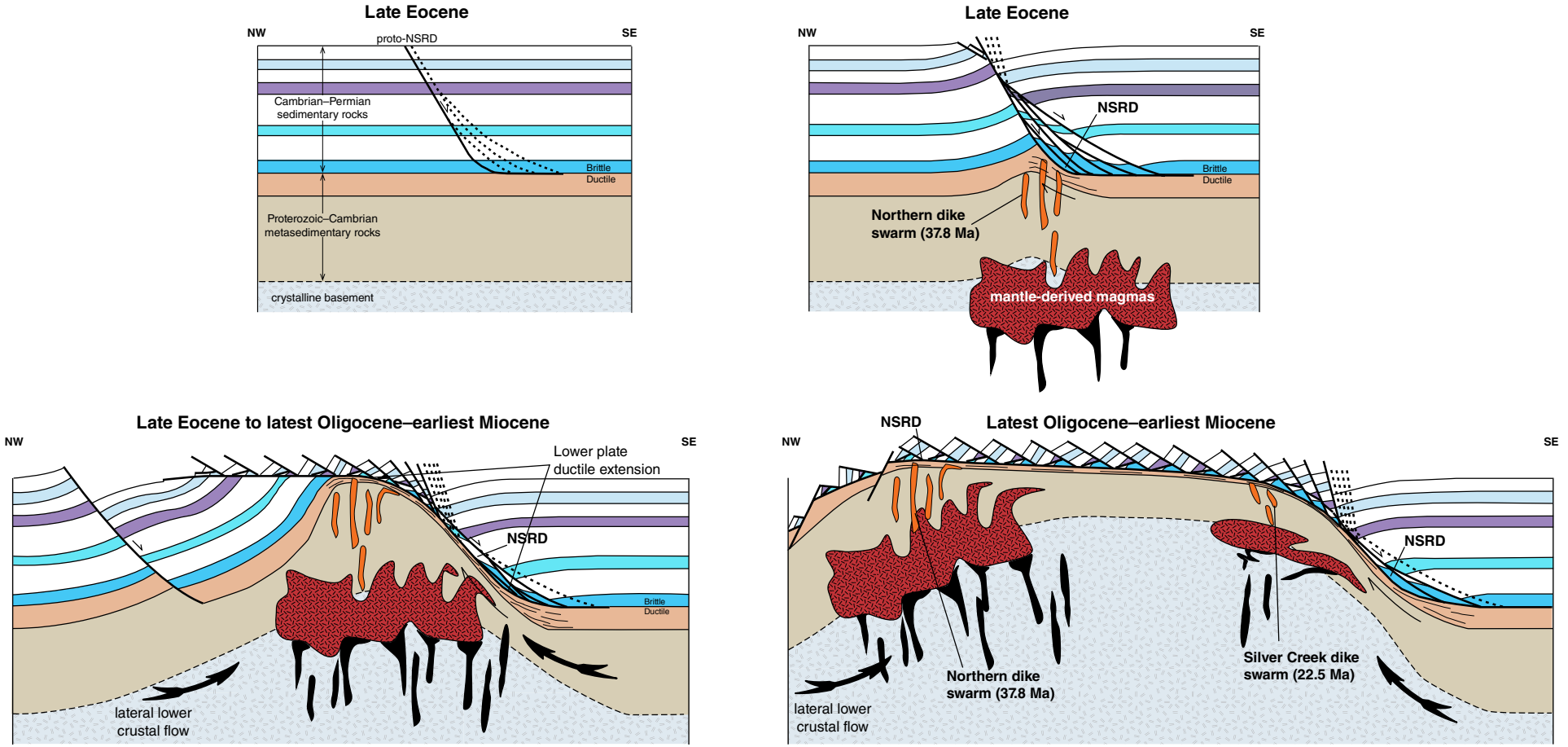

Figure 10. Schematic speculative evolutionary cross sections for the northern Snake Range metamorphic core complex (NSRD—northern Snake Range décollement). Modified from Johnston (2000), Miller et al. (1999a), and Gans et al. (1985).

cosity (e.g., Tullis et al., 1973; Koch et al., 1989), promoting ductile flow within these weak rocks during extensional deformation. In the models (e.g., Gessner et al., 2007; Rey et al., 2009a, 2009b; Whitney et al., 2013) ductile extensional flow is a response to isostatic unloading of the lower plate as space is created by thinned upper crust due to brittle extension.

To generate the detachment fault, numerical and analogue models require a preexisting local zone of weakness, i.e., a preexisting normal fault, a large density contrast across the brittle-ductile transition, or a rheologically weak zone (i.e., partial melt zone). In the northern half of the northern Snake Range, preextension thrust faults are exposed, but they dip west and are cut by the NSRD (Lee et al., 1999a; Lee and Gans, 1999); therefore, it appears unlikely that a preexisting thrust fault was reactivated as an east-dipping detachment fault. The juxtaposition of upper plate carbonates upon lower plate marbles, metapelites, and granitoids in the northern Snake Range indicates an absence of a large density contrast across the detachment. The lack of exposed Cenozoic plutons in the lower plate suggests that a local rheologically weak zone was not present in the northern Snake Range at the onset of extension. However, it is possible that late Eocene to Miocene plutons may be present just below exposures of the lower plate in the northern Snake Range (e.g., Miller et al., 1999a). Four observations support this inference: (1) exposures of late Eocene to Miocene rhyolite dikes in the northern Snake Range may be sourced from a pluton at depth; (2) there are exposures of late Eocene granitic plutons along strike to the north in the Kern Mountains and Deep Creek Range and to the south in the footwall of the southern Snake Range décollement (Miller et al., 1988) (Fig. 3); (3) isotopic data from east-central Nevada are interpreted as indicating a major influx of mantle-derived magmas into the crust during the late Eocene (Gottlieb and Miller, 2014; Gottlieb et al., 2015); and (4) interpretations of geophysical data indicate the presence of a buried pluton or plutons beneath the exposed southwestern section of the northern Snake Range (Grauch et al., 1988; Ponce, 1991; Mankinen et al., 2007). Therefore, if Cenozoic plutons are present at depth, they may be the source for the Northern and Silver Creek dike swarms we dated, and the heat of intrusion may have generated a rheologically weak zone that, in turn, triggered inception of detachment fault formation.

If late Eocene to latest Oligocene–earliest Miocene plutons were present during ductile extension, then the melt-present, slow strain rate (starting horizontal extension rate of 0.85 mm/yr) extension models of Rey et al. (2009a, 2009b) predict primary features of the northern Snake Range metamorphic core complex. These features include ductile deformation kinematics characterized by heterogeneous bulk flattening, except simple shear adjacent to the detachment fault, and extensional deformation that accommodates exhumation after cooling and crystallization of melt, resulting in a strongly deformed lower plate. One of the key parameters in this model is slow horizontal extensional strain rates. Extensional strain in the northern Snake Range may have been continuous or episodic, and if episodic, the timing of those episodes is not known; therefore, strain rates during ductile extensional deformation are not known.

Based on the energy feedback and localization numerical model of Rosenbaum et al. (2005), detachment faults can be generated in the absence of a preexisting zone of weakness. In this model, detachment-like faults developed within homogeneous hot crust of granitic composition in response to feedback between thermal elastic stresses, shear heating, elastic stored energy, and creep rheology. Detachment faults develop at the brittle-ductile transition zone where straining and shear localization is focused, dissipation of energy is at a maximum, and the zone weakens as a consequence of the thermal effects of shearing. The applicability of this model to the northern Snake Range is unlikely because the pre-Cenozoic geology was not homogeneous.

In nearly all of the models proposed for formation of detachment faults and metamorphic core complexes, i.e., early ones based on geometry and kinematics of extensional deformation (e.g., Wernicke, 1981; Miller et al., 1983; Buck, 1988), 2D thermal mechanical models (e.g., Gessner et al., 2007; Rey et al., 2009a, 2009b), 3D analogue models (e.g., Brun et al., 1994; Tirel et al., 2006), and energy constrained models (Rosenbaum et al., 2005), there is a close temporal and spatial link between upper crustal normal faulting, lower crustal ductile extension and flow, and detachment faulting. Thus, if any of these models apply to the northern Snake Range, the timing of upper crustal normal faulting must overlap with our constraints on the timing of ductile extension in the lower plate based on our new U/Pb zircon ages, combined with published muscovite $^{40}Ar/^{39}Ar$ thermochronology, MDD cooling histories, and zircon and apatite fission track thermochronology.

In the vicinity of the northern Snake Range (within a present-day distance of ~60 km), geologic mapping, stratigraphic studies, and geochronologic investigations on volcanic rocks and detrital zircons exposed within several sedimentary basins (blue stars in Fig. 2) shed light on the timing of formation of these sedimentary basins, their faulting histories, and the exhumation history of units that define the upper and lower plates (e.g., Drewes, 1967; Grier, 1984; Gans et al., 1989; Martinez et al., 1998; Martinez, 1999; Miller et al., 1999a; Ruksznis, 2015). In general, red beds or late Eocene (~35–40 Ma) air fall tuff are exposed at the base of these basins and unconformably overlie upper Paleozoic sedimentary rocks. Several observations, including red bed clasts locally derived from the underlying upper Paleozoic strata, the absence of detrital zircons from levels of the miogeoclinal stratigraphy deeper than the upper Paleozoic (Ruksznis, 2015), and a Paleogene paleogeographic reconstruction for eastern Nevada–western Utah (covering an area of ~60 km × 120 km approximately centered on the northern Snake Range) that shows exposures of Paleozoic rocks no older than Ordovician (Long, 2012), imply that strata no deeper than Ordovician Eureka Quartzite (~3.0–3.5 km stratigraphic depth within the miogeoclinal section; Ruksznis, 2015) were exposed at the surface in the vicinity of the northern Snake Range during the Eocene. Furthermore, Long's (2012) paleogeographic reconstruction shows evidence for prevolcanic to synvolcanic supracrustal extension during the Paleogene along as many as 70 relatively small offset normal faults (throws of ~1–2 km or less) and one interpreted normal fault with larger throw (~4 km) (Druschke et al., 2009a, 2009b, 2011).

Eocene exhumation and erosion of the upper ~3.0–3.5 km of the Paleozoic section from the footwall of a normal fault is comparable to exhumation of the lower plate of the northern Snake Range by ~3 km during the middle Eocene,

the interpreted first episode of Cenozoic exhumation in the lower plate based on MDD model cooling histories (Lee, 1995). This interpretation holds if the geothermal gradient during the Eocene was ~30 °C/km, i.e., the calculated Late Cretaceous to Paleocene geothermal gradient in central Nevada (Long et al., 2015) and the maximum typical for the Basin and Range today (Lachenbruch and Sass, 1978). Paleogene outcrop and exhumation data across east-central Nevada preclude widely distributed kilometer-scale slip on upper crustal normal faults of this age (Long, 2012; Ruksznis, 2015); however, normal fault slip and attendant topographic relief may have been locally significant between the Late Cretaceous and late Eocene (Long, 2012; Druschke et al., 2009a, 2009b, 2011). Thus, we postulate that a normal fault near the northern Snake Range, although not yet identified, accommodated Eocene upper crustal extension that accounted for the Eocene exhumation history recorded in lower plate rocks.

Across east-central Nevada in the vicinity of the northern Snake Range, the red beds or late Eocene tuff are overlain by tuffaceous sediments, ~7200 km^3 of late Eocene to early Oligocene andesite and dacite lavas and tuffs and rhyolite tuffs (Drewes, 1967; Gans et al., 1989; Grunder, 1992; Ruksznis, 2015), and early Miocene (ca. 21 Ma) tuffaceous lacustrine sediments, locally interlayered with rock avalanche deposits, and alluvial fan conglomerates (Grier, 1984; Gans et al., 1989; Martinez et al., 1998; Miller et al., 1999a; Ruksznis, 2015). Field observations show a small angular unconformity between the Eocene volcanic and sedimentary rocks and the base of the overlying tuffaceous lacustrine sediments, fanning dips upsection within the Miocene lacustrine sediments and overlying fanglomerates, and the first appearance of lower plate clasts in the fanglomerates during the early to middle Miocene (Miller et al., 1999a; Ruksznis, 2015). Together, these field relations suggest that the major phase of upper crustal normal faulting in east-central Nevada began with the formation of the tuffaceous lacustrine sediments during the early Miocene (Miller et al., 1999a; Ruksznis, 2015).

Zircon and apatite fission track and (U-Th)/He thermochronology data from footwall rocks to the NSRD, the southern Snake Range detachment fault, and the high-angle Basin and Range normal faults along the east flanks of the Deep Creek Range and Kern Mountains indicate that the major phase of Basin and Range normal fault slip occurred in the middle Miocene (ca. 17–15 Ma). Nevertheless, normal slip along the range-bounding faults likely spanned a longer time period, from ca. 23–21 to ca. 11–8 Ma, in part possibly overlapping with cessation of ductile extension in the lower plate of the northern Snake Range (Miller et al., 1999a; Metcalf, 2006; Evans et al., 2015). Combining our new U/Pb zircon data with these data, along with published moderate- to low-temperature thermochronologic data (Lee and Sutter, 1991; Lee, 1995; Gébelin et al., 2011), and timing of normal faulting and sedimentary basin formation in and around the northern Snake Range (Drewes, 1967; Grier, 1984; Gans et al., 1989; Martinez et al., 1998; Miller et al., 1999a; Ruksznis, 2015), indicates that our zircon age brackets for ductile extension in the lower plate overlap temporally with a minor phase of middle to late Eocene upper crustal extension in the vicinity of the northern Snake Range and the onset of the major episode of brittle extension during the early to middle Miocene (Fig. 9).

Thus, a plausible, but speculative, evolution for the northern Snake Range entails slip along a postulated late Eocene normal fault in the vicinity of the northern Snake Range that accommodated 3.0–3.5 km of vertical exhumation in its footwall, implying a horizontal extension magnitude of ~5–6 km assuming a 60° dipping fault (Fig. 10). To maintain strain compatibility, ~5–6 km of horizontal ductile extension in the middle crustal would need to have accumulated during the late Eocene, and such an amount represents ~30%–40% of the total horizontal ductile extension in the lower plate. In this scenario, the second pulse of lower plate horizontal ductile extension, i.e., 60%–70% of the total horizontal ductile extension, occurred in the latest Oligocene–earliest Miocene during or just prior to a pulse of rapid cooling of the lower plate (Lee, 1995) and the early stages of normal faulting along range-bounding faults extending from the Deep Creek Range south to the southern Snake Range (Fig. 2). This major phase of normal faulting reached its peak during the middle Miocene and was centered on the eastern flank of the range (Miller et al., 1999a) (Fig. 9), and appears to have resulted in ~10° of westward tilt of the lower plate, at least in the southeastern part of the range, as suggested by the 80° southeast-dipping Silver Creek dike swarm.

In this interpretation we assume that the lower plate metasedimentary sequence was at depths of 8–15 km in the Eocene, approximately half the depth during the late Mesozoic, as indicated by quantitative barometry of lower plate rocks on the east flank of range (Lewis et al., 1999; Cooper et al., 2010b). If our assumption is correct, it implies an episode of partial exhumation of the lower plate during the Late Cretaceous–Paleogene (Cooper et al., 2010b) that could be tied to evidence for similar age supracrustal extension in east-central Nevada (Long, 2012; Druschke et al., 2009a, 2009b).

In the Ruby Mountain–East Humboldt (REH) and Albion–Raft River–Grouse Creek (ARG) metamorphic core complexes, the timing of major phases of middle crustal ductile extensional deformation and exhumation is distinctly older than the major phase of upper crustal normal faulting. In the REH, lower plate ductile extension is ~10 m.y. older than the major phase of detachment faulting and associated high-angle normal faults (e.g., Colgan et al., 2010; Henry et al., 2011; Lund Snee et al., 2016, and references therein). In the ARG, lower plate ductile extension and shear along the overlying detachment faults are older, by as much as ~10–15 m.y., than high-angle normal faulting in the upper crust (e.g., Konstantinou et al., 2012, 2013, and references therein). The differences in the timing of middle crustal ductile extension and exhumation, detachment faulting, and upper crustal brittle normal faulting highlight a significant strain compatibility conundrum in that surface deformation appears to be minor during the major phase of middle crustal ductile extension and exhumation. To maintain strain compatibility, a decoupling zone between the ductilely extending middle crust and the essentially undeformed upper crust must be incorporated into any model developed to explain the formation of these metamorphic core complexes (Henry et al., 2011). A similar strain compatibility paradox exists for the northern Snake Range, unless the pre-Eocene extension allowable in Long's (2012) paleogeographic reconstruction accommodated exhumation of the lower plate from Cretaceous to Eocene depths.

CONCLUSIONS

We argue that our new field and petrography observations and ^{238}U-^{206}Pb zircon ages on the two rhyolite dike swarms, combined with published data on the (1) geology, structure, and kinematics of ductile and brittle extension, and the NSRD (Miller et al., 1983; Lee et al., 1987; Lee, 1990; Cooper et al., 2010a; Gébelin et al., 2011, 2014); (2) moderate- to low-temperature cooling histories in lower plate rocks of the northern Snake Range (Lee and Sutter, 1991; Lee, 1995; Miller et al., 1999a; Gébelin et al., 2011); and (3) distribution, age, geometry, and faulting histories of Cenozoic sedimentary and volcanic rocks in the vicinity of the northern Snake Range (Drewes, 1967; Grier, 1984; Gans et al., 1989; Martinez et al., 1998; Miller et al., 1999a; Ruksznis, 2015) are best interpreted as recording an episode of localized upper crustal brittle extension and vertical thinning during the late Eocene (Fig. 10). This deformation episode provided sufficient space to isostatically drive ductile extensional flow of hot and water-weakened middle crustal rocks upward from beneath the NSRD or proto-NSRD soon after, or simultaneously with, emplacement of the Northern dike swarm. The Northern dike swarm may be the shallower manifestation of mantle-derived magmas emplaced into deeper crust; these magmas provided the heat that rheologically weakened rocks now exposed in the lower plate (Fig. 10). Exhumation of the lower plate continued in a rolling hinge–isostatic rebound style, whereby the western part of the lower plate was exhumed first from depths and temperatures at which ductile extension occurred into the brittle crust in the footwall of the brittle NSRD. The eastern part of the lower plate remained at depth and at sufficiently high temperatures such that rocks extended ductilely either continuously or episodically until the latest Oligocene–earliest Miocene, whereupon the post-tectonic Silver Creek dike swarm was emplaced (Fig. 10). Exhumation of the lower plate toward the Earth's surface continued from the early to middle Miocene during a major episode of slip (vertical slip rate of ~1 mm/yr; Fig. 9) along the eastern part of the NSRD and associated high-angle normal faults.

ACKNOWLEDGMENTS

Lee received support for this research from a Blaustein Fellowship at the Stanford School of Earth Sciences; Johnston received postdoctoral support during collection of geochronology data as a researcher at the Arizona LaserChron Center. We thank Eric Gottlieb and Joe Wooden, who helped with cathodoluminescence imaging of zircons and analyzing them on the sensitive high-resolution ion microprobe (reverse geometry), and Gottlieb for digitally redrafting the base map in Figure 2. Discussions with Elizabeth Miller, Gottlieb, Carl Holland, Chris Henry, and Chris Mattinson, comments on an earlier version of this manuscript by Miller; and review comments from Allen McGrew and Christian Teyssier and editors Terry Pavlis and Shan de Silva improved the clarity of our ideas.

REFERENCES CITED

Baldwin, S.L., and Lister, G.S., 1998, Thermochronology of the South Cyclades shear zone, Ios, Greece, effects of ductile shear in the argon partial retention zone: Journal of Geophysical Research, v. 103, p. 7315–7336, doi:10.1029/97JB03106.

Bartley, J.M., and Wernicke, B.P., 1984, The Snake Range décollement interpreted as a major extensional shear zone: Tectonics, v. 3, p. 647–657, doi:10.1029/TC003i006p00647.

Beltrando, M., Lister, G.S., Forster, M., Dunlap, W.J., Fraser, G., and Hermann, J., 2009, Dating microstructures by the $^{40}Ar/^{39}Ar$ step-heating technique: Deformation-pressure-temperature-time history of the Penninic units of the Western Alps: Lithos, v. 113, p. 801–819, doi:10.1016/j.lithos.2009.07.006.

Brandon, M.T., and Vance, J.A., 1992, New statistical methods for analysis of fission track grain age distributions with applications to detrital zircon ages from the Olympic subduction complex, western Washington State: American Journal of Science, v. 292, p. 565–636, doi:10.2475/ajs.292.8.565.

Brun, J.-P., Sokoutis, D., and van den Driessche, J., 1994, Analogue modeling of detachment fault systems and core complex: Geology, v. 22, p. 319–322, doi:10.1130/0091-7613(1994)022<0319:AMODFS>2.3.CO;2.

Buck, W.R., 1988, Flexural rotation of normal faults: Tectonics, v. 7, p. 959–973, doi:10.1029/TC007i005p00959.

Burkhard, M., 1993, Calcite twins, their geometry, appearance and significance as stress-strain markers and indicators of tectonic regime: A review: Journal of Structural Geology, v. 15, p. 351–368, doi:10.1016/0191-8141(93)90132-T.

Colgan, J.P., Howard, K.A., Fleck, R.J., and Wooden, J.L., 2010, Rapid middle Miocene extension and unroofing of the southern Ruby Mountains, Nevada: Tectonics, v. 29, TC6022, doi:10.1029/2009TC002655.

Coney, P.J., and Harms, T.A., 1984, Cordilleran metamorphic core complexes: Cenozoic extensional relics of Mesozoic compression: Geology, v. 12, p. 550–554, doi:10.1130/0091-7613(1984)12<550:CMCCCE>2.0.CO;2.

Cooper, F.J., Platt, J.P., Platzman, E.S., Grove, M.J., and Seward, G., 2010a, Opposing shear senses in a subdetachment mylonite zone: Implications for core complex mechanics: Tectonics, v. 29, TC4019, doi:10.1029/2009TC002632.

Cooper, F.J., Platt, J.P., Anczkiewicz, R., and Whitehouse, M.J., 2010b, Footwall dip of a core complex detachment fault: Thermobarometric constraints from the northern Snake Range (Basin and Range, USA): Journal of Metamorphic Geology, v. 28, p. 997–1020, doi:10.1111/j.1525-1314.2010.00907.x.

Corti, G., Bonini, M., Conticelli, S., Innocenti, F., Manetti, P., and Sokoutis, D., 2003, Analogue modelling of continental extension: A review focused on the relations between the patterns of deformation and the presence of magma: Earth-Science Reviews, v. 63, p. 169–247, doi:10.1016/S0012-8252(03)00035-7.

Drewes, H., 1967, Geology of the Connors Pass Quadrangle, Schell Creek Range, East-Central Nevada: U.S. Geological Survey Professional Paper 557, 93 p.

Druschke, P., Hanson, A.D., Wells, M.L., Rasbury, T., Stöckli, D., and Gehrels, G., 2009a, Synconvergent surface-breaking normal faults of Late Cretaceous age within the Sevier hinterland, east-central Nevada: Geology, v. 37, p. 447–450, doi:10.1130/G25546A.1.

Druschke, P., Hanson, A.D., and Wells, M.L., 2009b, Structural, stratigraphic, and geochronologic evidence for extension predating Paleogene volcanism in the Sevier hinterland, east-central Nevada: International Geology Review, v. 51, p. 743–775, doi:10.1080/00206810902917941.

Druschke, P., Hanson, A.D., Wells, M.L., Gehrels, G.E., and Stockli, D., 2011, Paleogeographic isolation of the Cretaceous to Eocene Sevier hinterland, east-central Nevada: Insights from U-Pb and (U-Th)/He detrital zircon ages of hinterland strata: Geological Society of America Bulletin, v. 123, p. 1141–1160, doi:10.1130/B30029.1.

Evans, S.L., Styron, R.H., van Soest, J.C., Hodges, K.V., and Hanson, A.D., 2015, Zircon and apatite (U-Th)/He evidence for Paleogene and Neogene extension in the southern Snake Range, Nevada, USA: Tectonics, v. 34, p. 2142–2164, doi:10.1002/2015TC003913.

Ferrill, D.A., Morris, A.P., Evans, M.A., Burkhard, M., Groshong, R.H., and Onasch, C.M., 2004, Calcite twin morphology: A low-temperature deformation geothermometer: Journal of Structural Geology, v. 26, p. 1521–1529, doi:10.1016/j.jsg.2003.11.028.

Foster, D.A., Kohn, B.P., and Gleadow, A.J.W., 1996, Sphene and zircon fission track closure temperatures revisited; empirical calibrations from $^{40}Ar/^{39}Ar$ diffusion studies of K-feldspar and biotite, *in* International Workshop on Fission Track Dating, Abstracts: Gent, University of Gent, p. 37.

Gans, P.B., Miller, E.L., McCarthy, J., and Oldcott, M.L., 1985, Tertiary extensional faulting and evolving ductile brittle transition zones in the northern Snake Range and vicinity: New insights from seismic data: Geology, v. 13, p. 189–193, doi:10.1130/0091-7613(1985)13<189:TEFAED>2.0.CO;2.

Gans, P.B., Mahood, G.A., and Schermer, E., 1989, eds., Synextensional Magmatism in the Basin and Range Province: A Case Study from the Eastern Great Basin: Geological Society of America Special Paper 233, 53 p., doi:10.1130/SPE233-p1.

Gans, P.B., Miller, E.L., and Lee, J., 1999a, Geologic Map of the Spring Mountain Quadrangle, Nevada and Utah: Nevada Bureau of Mines and Geology Field Studies Map 18, scale 1:24,000, 12 p.

Gans, P.B., Miller, E.L., Huggins, C.C., and Lee, J., 1999b, Geologic Map of the Little Horse Canyon Quadrangle, Nevada and Utah: Nevada Bureau of Mines and Geology Field Studies Map 20, scale 1:24,000, 12 p.

Gaudemer, Y., and Tapponnier, P., 1987, Ductile and brittle deformations in the northern Snake Range, Nevada: Journal of Structural Geology, v. 9, p. 159–180, doi:10.1016/0191-8141(87)90023-X.

Gébelin, A., Mulch, A., Teyssier, C., Heizler, M., Vennemann, T., and Seaton, N.C.A., 2011, Oligo-Miocene extensional tectonics and fluid flow across the northern Snake Range detachment system, Nevada: Tectonics, v. 30, TC5010, doi:10.1029/2010TC002797.

Gébelin, A., Teyssier, C., Heizler, M., and Mulch, A., 2014, Meteoric water circulation in a rolling-hinge detachment system (northern Snake Range core complex, Nevada): Geological Society of America Bulletin, v. 127, p. 149–161, doi:10.1130/B31063.1.

Gehrels, G.E., Valencia, V.A., and Ruiz, J., 2008, Enhanced precision, accuracy, efficiency, and spatial resolution of U-Pb ages by laser ablation–multicollector–inductively coupled plasma–mass spectrometry: Geochemistry, Geophysics, and Geosystems, v. 9, Q03017, doi:10.1029/2007GC001805.

Gessner, K., Wijns, C., and Moresi, L., 2007, Significance of strain localization in the lower crust for structural evolution and thermal history of metamorphic core complexes: Tectonics, v. 26, TC2012, doi:10.1029/2004TC001768.

Gottlieb, E.S., and Miller, E.L., 2014, Zircon xenocryst evidence of magmatic mobilization and homogenization of east central Nevada deep crust during the Eocene magmatic sweep: Geological Society of America Abstracts with Programs, v. 46, no. 5, p. 73.

Gottlieb, E.S., Miller, E.L., Valley, J.W., and Kitajima, K., 2015, Light $\delta^{18}O$ zircon xenocrysts from the deep crust of the Great Basin, North American Cordillera: Goldschmidt 2015 Abstracts, no. 1083.

Grier, S., 1984, Alluvial fan and lacustrine carbonate deposits in the Snake Range: A study of Tertiary sedimentation and associated tectonism [M.S. thesis]: Stanford, California, Stanford University, 61 p.

Grauch, V.J.S., Blakely, R.J., Blank, H.R., Oliver, H.W., Plouff, D., and Ponce, D.A., 1988, Geophysical Delineation of Granitic Plutons in Nevada: U.S. Geological Survey Open-File Report 88-11, scale 1:1,000,000, 7 p.

Grunder, A.L., 1992, Two-stage contamination during crustal assimilation: Isotopic evidence from volcanic rocks in eastern Nevada: Contributions to Mineralogy and Petrology, v. 112, p. 219–229, doi:10.1007/BF00310456.

Harrison, T.M., and Zeitler, P.K., 2005, Fundamentals of noble gas thermochronometry: Reviews in Mineralogy and Geochemistry, v. 58, p. 123–149, doi:10.2138/rmg.2005.58.5.

Harrison, T.M., Célérier, J., Aikman, A.B., Hermann, J., and Heizler, M.T., 2009, Diffusion of ^{40}Ar in muscovite: Geochimica et Cosmochimica Acta, v. 73, p. 1039–1051, doi:10.1016/j.gca.2008.09.038.

Henry, C.D., McGrew, A.J., Colgan, J.P., Snoke, A.W., and Brueseke, M., 2011, Timing, distribution, amount, and style of Cenozoic extension in the northern Great Basin, *in* Lee, J., and Evans, J.P., eds., Geologic Field Trips to the Basin and Range, Rocky Mountains, Snake River Plain, and Terranes of the U.S. Cordillera: Geological Society of America Field Guide 21, p. 27–66, doi:10.1130/2011.0021(02).

Jackson, J.A., 1987, Active normal faulting and crustal extension, *in* Coward, M.P., Dewey, J.F., and Hancock, P.L., eds., Continental Extensional Tectonics: Geological Society of London Special Publication 28, p. 3–17, doi:10.1144/GSL.SP.1987.028.01.02.

Jaffey, A.H., Flynn, K.F., Glendenin, L.E., Bentley, W.C. and Essling, A.M., 1971, Precision measurements of half-lives and specific activities of ^{235}U and ^{238}U: Physical Reviews C, v. 4, p. 1889–1906, doi:10.1103/PhysRevC.4.1889.

Johnston, S.M., 2000, Normal faulting in the upper plate of a metamorphic core complex, northern Snake Range, Nevada [M.S. thesis]: Stanford, California, Stanford University, 60 p.

Kirschner, D.L., Cosca, M.A., Masson, H., and Hunziker, J.C., 1996, Staircase $^{40}Ar/^{39}Ar$ spectra of fine-grained white mica: Timing and duration of deformation and empirical constraints on argon diffusion: Geology, v. 24, p. 747–750, doi:10.1130/009–7613(1996)024<0747:SAASOF>2.3.CO;2.

Koch, P.S., Christie, J.M., Ord, A., and George, R.P.J., 1989, Effect of water on the rheology of experimentally deformed quartzite: Journal of Geophysical Research, v. 94, p. 13,975–13,996, doi:10.1029/JB094iB10p13975.

Konstantinou, A., and Miller, E., 2015, Evidence for a long-lived accommodation/transfer zone beneath the Snake River Plain: A possible influence on Neogene magmatism?: Tectonics, v. 34, p. 2387–2398, doi:10.1002/2015TC003863.

Konstantinou, A., Strickland, A., Miller, E.L., and Wooden, J.W., 2012, Multi-stage Cenozoic extension of the Albion–Raft River–Grouse Creek metamorphic core complex: Geochronologic and stratigraphic constraints: Geosphere, v. 8, p. 1429–1466, doi:10.1130/GES00778.1.

Konstantinou, A, Strickland, A., Miller, E., Vervoort, J., Fisher, C.M., Wooden, J., and Valley, J., 2013, Synextensional magmatism leading to crustal flow in the Albion-Raft River-Grouse Creek metamorphic core complex, northeastern Basin and Range: Tectonics, v. 32, 1384–1403, doi:10.1002/tect.20085.

Kula, J., and Spell, T.L., 2012, Recovery of muscovite age gradients by $^{40}Ar/^{39}Ar$ vacuum furnace step-heating analysis: Chemical Geology, v. 304–305, p. 166–174, doi:10.1016/j.chemgeo.2012.02.013.

Kula, J., Spell, T.L., and Zanetti, K.A., 2010, $^{40}Ar/^{39}Ar$ analyses of artificially mixed micas and the treatment of complex age spectra from samples with multiple mica populations: Chemical Geology, v. 275, p. 67–77, doi:10.1016/j.chemgeo.2010.04.015.

Lachenbruch, A.H., and Sass, J.H., 1978, Models of an extending lithosphere and heat flow in the Basin and Range province, *in* Smith, R.B., and Eaton, G.P., eds., Cenozoic Tectonics and Regional Geophysics at the Western Cordillera: Geological Society of America Memoir 152, p. 209–250, doi:10.1130/MEM152-p209.

Lavier, L.L., Buck, W.R., and Poliakov, A.N.B., 1999, Self-consistent rolling-hinge model for the evolution of large-offset, low-angle normal faults: Geology, v. 27, p. 1127–1130, doi:10.1130/0091-7613(1999)027<1127:SCRHMF>2.3.CO;2.

Lavier, L.L., Buck, W.R., and Poliakov, A.N.B., 2000, Factors controlling normal fault offset in an ideal brittle layer: Journal of Geophysical Research, v. 105, p. 23,431–23,442, doi:10.1029/2000JB900108.

Lee, D.E., and Fischer, L.B., 1985, Cretaceous metamorphism in the northern Snake Range, Nevada, a metamorphic core complex: Isochron-West, v. 42, p. 3–7.

Lee, J., 1990, Structural Geology and $^{40}Ar/^{39}Ar$ Thermochronology of the Northern Snake Range, Nevada [Ph.D. thesis]: Stanford, California, Stanford University, 184 p.

Lee, J., 1995, Rapid uplift and rotation of mylonites: Insights from potassium feldspar $^{40}Ar/^{39}Ar$ thermochronology, northern Snake Range, Nevada: Tectonics, v. 14, p. 54–77, doi:10.1029/94TC01508.

Lee, J., and Gans, P.B., 1999, Geologic Map of the Mormon Jack Pass Quadrangle, Nevada: Nevada Bureau of Mines and Geology Field Studies Map 17, scale 1:24,000, 12 p.

Lee, J., and Sutter, J.F., 1991, Incremental $^{40}Ar/^{39}Ar$ thermochronology of mylonitic rocks from the northern Snake Range, Nevada: Tectonics, v. 10, p. 77–100, doi:10.1029/90TC01931.

Lee, J., Miller, E.L., and Sutter, J.F., 1987, Ductile strain and metamorphism in an extensional tectonic setting: A case study from the northern Snake Range, Nevada, U.S.A., *in* Coward, M.P., et al., eds., Continental Extensional Tectonics: Geological Society of London Special Publication 28, p. 267–298, doi:10.1144/GSL.SP.1987.028.01.18.

Lee, J., Gans, P.B., and Miller, E.L., 1999a, Geologic Map of the Third Butte East Quadrangle, Nevada: Nevada Bureau of Mines and Geology Field Studies Map 16, scale 1:24,000, 12 p.

Lee, J., Miller, E.L., Gans, P.B., and Huggins, C.C., 1999b, Geologic Map of the Mount Moriah Quadrangle, Nevada: Nevada Bureau of Mines and Geology, Field Studies Map 19, scale 1:24,000, 12 p.

Lewis, C.J., Wernicke, B.P., Selverstone, J., and Bartley, J.M., 1999, Deep burial of the footwall of the northern Snake Range décollement, Nevada: Geological Society of America Bulletin, v. 111, p. 39–51, doi:10.1130/0016-7606(1999)111<0039:DBOTFO>2.3.CO;2.

Lister, G.S., and Davis, G.A., 1989, The origin of metamorphic core complexes and detachment faults formed during Tertiary continental extension in the northern Colorado River region, U.S.A.: Journal of Structural Geology, v. 11, p. 65–94, doi:10.1016/0191-8141(89)90036-9.

Little, T.A., Mortimer, N., and McWilliams, M., 1999, An episodic Cretaceous cooling model for the Otago-Marlborough Schist, New Zealand, based on $^{40}Ar/^{39}Ar$ white mica ages: New Zealand Journal of Geology and Geophysics, v. 42, p. 305–325, doi:10.1080/00288306.1999.9514848.

Long, S.P., 2012, Magnitudes and spatial patterns of erosional exhumation in the Sevier hinterland, eastern Nevada and western Utah, USA: Insights from a Paleogene paleogeologic map: Geosphere, v. 8, p. 881–901, doi:10.1130/GES00783.1.

Long, S.P., Thomson, S.N., Reiners, P.W., and Di Fiori, R.V., 2015, Synorogenic extension localized by upper-crustal thickening: An example from the Late Cretaceous Nevadaplano: Geology, v. 43, p. 351–354, doi:10.1130/G36431.1.

Ludwig, K., 2003, User's Manual for Isoplot 3.00: A Geochronological Toolkit for Microsoft Excel: Berkeley Geochronology Center Special Publication 4.

Lund Snee, J.-E., Miller, E.L., Grove, J., Hourigan, J.K., and Konstantinou, A., 2016, Cenozoic paleogeographic evolution of the Elko Basin and surrounding region, northeast Nevada, Geosphere, v. 12, p. 464–500, doi:10.1130/GES01198.1.

Mankinen, E.A., Roberts, C.W., McKee, E.H., Chuchel, B.A., and Morin, R.L., 2007, Geophysical Data from Spring Valley to Delamar Valley, East-Central Nevada: U.S. Geological Survey Open-File Report 2007-1190, 42 p.

Martinez, C.M., 1999, Tertiary sedimentation in the Sacramento Pass Basin, east-central Nevada: Implications for the evolution of extensional detachment faults in the Basin and Range: American Association of Petroleum Geologists Bulletin, v. 83, p. 1891.

Martinez, C.M., Miller, E.L., and Stockli, D.F., 1998, Miocene age rock avalanche deposits of the Sacramento Pass Basin, Basin and Range Province, Nevada: Geological Society of America Abstracts with Programs, v. 30, no. 5, p. 53.

Mattinson, J.M., 2005, Zircon U-Pb chemical abrasion ("CA-TIMS") method: Combined annealing and multi-step partial dissolution analysis for improved precision and accuracy of zircon ages: Chemical Geology, v. 220, p. 47–66, doi:10.1016/j.chemgeo.2005.03.011.

Metcalf, J.R., 2006, Constraining continental deformation with the apatite (U-Th)/He thermochronometer [Ph.D. thesis]: Stanford, California, Stanford University, 135 p.

Miller, E.L., and Gans, P.B., 1989, Cretaceous crustal structure and metamorphism in the hinterland of the Sevier thrust belt, western U.S. Cordillera: Geology, v. 17, p. 59–62, doi:10.1130/0091-7613(1989)017<0059:CCSAMI>2.3.CO;2.

Miller, E.L., and Gans, P.B., 1999, Geologic Map of the Cove Quadrangle, Nevada: Nevada Bureau of Mines and Geology Field Studies Map 22, scale 1:24,000, 12 p.

Miller, E.L., Gans, P.B., and Garing, J.D., 1983, The Snake Range decollement: An exhumed mid-Tertiary ductile-brittle transition: Tectonics, v. 2, p. 239–263, doi:10.1029/TC002i003p00239.

Miller, E.L., Gans, P.B., Wright, J.E., and Sutter, J.F., 1988, Metamorphic history of the east-central Basin and Range Province: Tectonic setting and relationship to magmatism, *in* Ernst, W.G., ed., Metamorphism and Crustal Evolution of the Western United States: Rubey Volume VII: Englewood Cliffs, New Jersey, Prentice-Hall, p. 649–682.

Miller, E.L., Dumitru, T.A., Brown, R.W., and Gans, P.B., 1999a, Rapid Miocene slip on the Snake Range–Deep Creek range fault system, east-central Nevada: Geological Society of America Bulletin, v. 111, p. 886–905, doi:10.1130/0016-7606(1999)111<0886:RMSOTS>2.3.CO;2.

Miller, E.L., Gans, P.B., Huggins, C.C., Grier, S.P., and Lee, J., 1999b, Geologic Map of the Old Mans Canyon Quadrangle, Nevada and Utah: Nevada Bureau of Mines and Geology Field Studies Map 21, scale 1:24,000, 12 p.

Passchier, C.W., and Trouw, R.A.J., 2005, Microtectonics: Berlin, Springer, 366 p.

Ponce, D.A., 1991, Gravity and magnetic anomalies in the Ely quadrangle, Nevada, and anomalies related to granitic plutons, *in* Raines, G.L., ed., Geology and Ore Deposits of the Great Basin: Symposium Proceedings: Reno, Geological Society of Nevada, p. 103–106.

Rahn, M.K., Brandon, M.T., Batt, G.E., and Garver, J.I., 2004, A zero-damage model for fission-track annealing in zircon: American Mineralogist, v. 89, p. 473–484, doi:10.2138/am-2004-0401.

Renne, P.R., Swisher, C.C., Deino, A.L., Karner, D.B., Owens, T.L., and DePaolo, D.J., 1998, Intercalibration of standards, absolute ages and uncertainties in $^{40}Ar/^{39}Ar$ dating: Chemical Geology, v. 145, p. 117–152, doi:10.1016/S0009-2541(97)00159-9.

Rey, P.F., Teyssier, C., and Whitney, D.L., 2009a, Extension rates, crustal melting, and core complex dynamics: Geology, v. 37, p. 391–394, doi:10.1130/G25460A.1.

Rey, P.F., Teyssier, C., and Whitney, D.L., 2009b, The role of partial melting and extensional strain rates in the development of metamorphic core complexes; hot orogens: Tectonophysics, v. 477, p. 135–144, doi:10.1016/j.tecto.2009.03.010.

Rey, P.F., Teyssier, C., Kruckenberg, S.C., and Whitney, D.L., 2011, Viscous collision in channel explains double domes in metamorphic core complexes: Geology, v. 39, p. 387–390, doi:10.1130/G31587.1.

Rosenbaum, G., Regenauer-Lieb, K., and Weinberg, R., 2005, Continental extension: From core complexes to rigid block faulting: Geology, v. 33, p. 609–612, doi:10.1130/G21477.1.

Ruksznis, A., 2015, Geology and geochronology of Cenozoic sedimentary basins, east-central Nevada [M.S. thesis]: Stanford, California, Stanford University, 229 p.

Tagami, T., and Dumitru, T.A., 1996, Provenance and thermal history of the Franciscan accretionary complex: Constraints from zircon fission track thermochronology: Journal of Geophysical Research, v. 101, p. 11353–11364, doi:10.1029/96JB00407.

Tirel, C., Brun, J.P., and Sikoutis, D., 2006, Extension of thickened and hot lithospheres: Inferences from laboratory modeling: Tectonics, v. 25, TC1005, doi:10.1029/2005TC001804.

Tirel, C., Brun, J.-P., and Burov, E., 2008, Dynamics and structural development of metamorphic core complexes: Journal of Geophysical Research, v. 113, B04403, doi:10.1029/2005JB003694.

Tullis, J.A., Christie, J.M., and Griggs, D.T., 1973, Microstructures and preferred orientations of experimentally deformed quartzites: Geological Society of America Bulletin, v. 84, p. 297–314, doi:10.1130/0016-7606(1973)84<297:MAPOOE>2.0.CO;2.

Vogl, J.J., Foster, D.A., Fanning, C.M., Kent, K.A., Rodgers, D.W., and Diedesch, T., 2012, Timing of extension in the Pioneer metamorphic core complex with implications for the spatial-temporal pattern of Cenozoic extension and exhumation in the northern U.S. Cordillera: Tectonics, v. 31, TC1008, doi:10.1029/2011TC002981.

Wells, M.L., Hoisch, T.D., Cruz-Uribe, A.M., and Vervoort, J.D., 2012, Geodynamics of synconvergent extension and tectonic mode switching: Constraints from the Sevier-Laramide orogen: Tectonics, v. 31, TC1002, doi:10.1029/2011TC002913.

Wernicke, B., 1981, Low-angle normal faults in the Basin and Range Province: Nappe tectonics in an extending orogen: Nature, v. 291, p. 645–648, doi:10.1038/291645a0.

Wernicke, B., and Axen, G.J., 1988, On the role of isostasy in the evolution of normal fault systems: Geology, v. 16, p. 848–851, doi:10.1130/0091-7613(1988)016<0848:OTROII>2.3.CO;2.

Whitney, D.L., Teyssier, C., Rey, P., and Buck, W.R., 2013, Continental and oceanic core complexes: Geological Society of America Bulletin, v. 125, p. 273–298, doi:10.1130/B30754.1.

Wijbrans, J.R., and McDougall, I., 1986, $^{40}Ar/^{39}$dating of white micas from an Alpine high-pressure metamorphic belt on Naxos (Greece): The resetting of the argon isotopic system: Contributions to Mineralogy and Petrology, v. 93, p. 187–194, doi:10.1007/BF00371320.

Wijns, C., Weinberg, R., Gessner, K., and Moresi, L., 2005, Mode of crustal extension determined by rheological layering: Earth and Planetary Science Letters, v. 236, p. 120–134, doi:10.1016/j.epsl.2005.05.030.

Williams, I.S., 1998, U-Th-Pb geochronology by ion microprobe, *in* McKibben, M.A., Shanks III, W.C., and Ridley, W.I., eds., Applications of Microanalytical Techniques to Understanding Mineralizing Processes: Reviews in Economic Geology Special Publication, v. 7, p. 1–35.